



High-resolution Spectroscopic Analysis of Four Unevolved Barium Stars*

M. P. Roriz¹, N. Holanda¹, L. V. da Conceição², S. Junqueira¹, N. A. Drake^{1,3}, A. Sonally¹, and C. B. Pereira¹¹ Observatório Nacional/MCTI, Rua General José Cristino, 77, 20921-400, Rio de Janeiro, Brazil; michelle@on.br² Department of Physics and Astronomy, University of Manitoba, Winnipeg, MB, R3T 2N2, Canada³ Laboratory of Observational Astrophysics, Saint Petersburg State University, Universitetski pr. 28, 198504, Saint Petersburg, Russia

Received 2023 March 12; revised 2024 January 30; accepted 2024 February 14; published 2024 March 28

Abstract

A classical local thermodynamic equilibrium analysis, based on high-resolution spectroscopic data, is performed for a sample of three potential barium dwarf candidates and one star already recognized as such. We derived their atmospheric parameters, estimated their masses and luminosities, and determined chemical abundances for a set of 21 elements, including CNO. Some elemental abundances are derived for the first time in HD 15096, HD 37792, and HD 141804. The program stars are dwarfs/subgiants with metallicities typical of disk stars, exhibiting moderate carbon enhancements, with [C/Fe] ratios ranging from +0.29 to +0.66 dex, and high levels of *s*-process elements, with [s/Fe] \gtrsim +1.0 dex. As spectroscopic binaries, their peculiarities are attributable to mass transfer events. The observed neutron-capture patterns were individually compared with two sets of *s*-process nucleosynthesis models (Monash and FRUITY), yielding dilution factors and masses estimates for the former polluting asymptotic giant branch stars. Low-mass ($\lesssim 3.0 M_{\odot}$) models successfully reproduce the observations. In addition, we estimated mean neutron exposures on the order of 0.6–0.7 mb⁻¹ for the *s*-processed material observed in their envelopes. Applying an empirical initial-final mass relation, we constraint in $\sim 0.7 M_{\odot}$ the mass of their dim white dwarf companions. Moreover, our kinematic study revealed that the program stars are members of the thin disk, with probabilities greater than 70%. Hence, we identified HD 15096 and HD 37792 as new barium dwarfs and confirmed that HD 141804 is a barium dwarf. Thus, the number of barium dwarfs identified in the literature from high-resolution spectroscopy increases to 71 objects.

Unified Astronomy Thesaurus concepts: [Fundamental parameters of stars \(555\)](#); [Stellar atmospheres \(1584\)](#); [Stellar abundances \(1577\)](#); [Chemically peculiar stars \(226\)](#); [Spectroscopy \(1558\)](#)

Supporting material: machine-readable tables

1. Introduction

Barium (Ba) stars (Bidelman & Keenan 1951) and their Population II analogs, CH stars (Keenan 1942), were initially recognized as red giants enriched in carbon and elements synthesized mostly through the *s*-process neutron-capture mechanism (*s*-process; Burbidge et al. 1957; Käppeler et al. 2011; Lugaro et al. 2023). However, the *s*-process nucleosynthesis is expected to take place in the interiors of thermally pulsing asymptotic giant branch (TP-AGB) stars (Gallino et al. 1998; Busso et al. 1999; Straniero et al. 2006; Karakas & Lattanzio 2014). Consequently, as first ascent giants, Ba and CH stars are not able to produce in loco and self-enrich their envelopes with the *s*-processed material. Until the discovery of their binary nature (McClure et al. 1980; McClure 1984; McClure & Woodsworth 1990), such peculiarities posed a challenge to the early stellar evolution models.

Belonging to binary systems, the chemical anomalies observed in Ba and related stars are attributed to mass exchange effects. In the framework of post-mass-transfer interacting binaries, the primary TP-AGB star loses mass and pollutes the atmosphere of its less evolved companion. As the

secondary star evolves, it becomes an *s*-rich giant, observed as a Ba/CH star, depending on the metallicity, while the former TP-AGB ends as a dim white dwarf (WD). Over the years, detailed chemical abundance analyses have confirmed the *s*-rich nature of Ba stars (Allen & Barbuy 2006a; Pereira et al. 2011; de Castro et al. 2016; Karinkuzhi et al. 2018b; Shejeelammal et al. 2020; Roriz et al. 2021a, 2021b) and CH stars (Goswami et al. 2006, 2016; Karinkuzhi & Goswami 2014, 2015; Purandardas et al. 2019). Moreover, their binary nature is widely supported by data acquired from extensive programs of radial velocity monitoring (Jorissen et al. 1998, 2019). As post-mass-transfer binaries, Ba/CH stars provide valuable observational constraints to *s*-process nucleosynthesis models in AGB stars (e.g., Cseh et al. 2018, 2022), binary star evolution models (e.g., Escorza et al. 2020), and the mass-transfer mechanisms (e.g., Jorissen et al. 1998, 2016).

1.1. Barium Dwarf Stars

In addition to explaining the origins of Ba/CH giants, the mass-transfer scenario also predicts the existence of less evolved analog stars exhibiting in their envelopes the Ba II syndrome observed in the classical giants. Indeed, the discovery of the so-called “CH subgiant stars” (Bond 1974; Luck & Bond 1982, 1991) and the F/G-type main-sequence Ba dwarf stars (Tomkin et al. 1989; North et al. 1994), thought to be linked to classical giants (see, e.g., Escorza et al. 2020), provided observational evidence in this sense.

Despite their nomenclatures, Ba dwarfs and CH subgiants exhibit many similarities. They share the same region in the HR

* HD 15096, HD 37792, and HD 141804 were observed under the program ID 097.A-9024(A). HD 207585 was observed under the agreement between Observatório Nacional (Brazil) and the European Southern Observatory (ESO).



Original content from this work may be used under the terms of the [Creative Commons Attribution 4.0 licence](#). Any further distribution of this work must maintain attribution to the author(s) and the title of the work, journal citation and DOI.

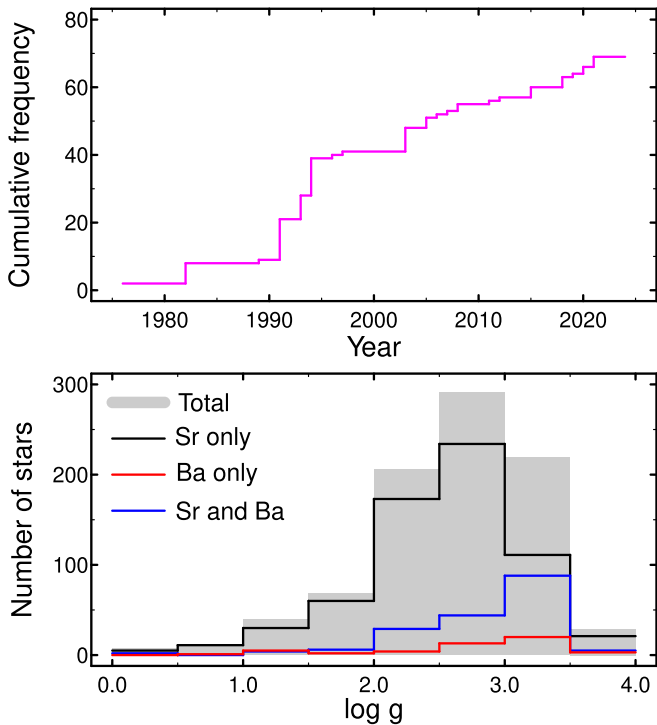


Figure 1. Upper panel: temporal evolution of the cumulative frequency of Ba dwarf stars confirmed from detailed chemical analyses. Bottom panel: distribution of the 895 *s*-process-rich candidates (gray) reported by Norfolk et al. (2019), identifying the subsample labeled as Sr only (black), Ba only (red), and Sr and Ba (blue). Stars with $\log g \geq 3.5$ represent only $\sim 0.3\%$ of the total number of candidates.

diagram (Escorza et al. 2017) and exhibit no clear distinction in the period–eccentricity diagram (Escorza et al. 2019; North et al. 2020). From a chemical point of view, studies based on high-resolution spectroscopy point to the chemical similarity between Ba dwarfs and CH subgiants (Pereira & Junqueira 2003; Pereira 2005; Allen & Barbuy 2006a). These systems are generally referred to as Ba dwarfs and, just like classical giants, also help us to trace back their former TP-AGB polluters, figuring as powerful tracers of the *s*-process nucleosynthesis.

However, Ba dwarfs turned out to be rare objects, calling into question whether they are the progenitors of Ba/CH giants (e.g., Luck & Bond 1991). In light of the mass-transfer hypothesis, the former are expected to be as common as the latter (Frantsman 1992; Han et al. 1995). A search of the literature reveals that the current sample of Ba dwarfs, confirmed from detailed chemical analyses, comprises only 69 stars. This is a relatively small number, compared to the current sample of Ba giants studied from high-resolution spectroscopy; for example, de Castro et al. (2016) reported an analysis of 169 Ba giants.

Moreover, as illustrated in the upper panel of Figure 1, the number of Ba dwarfs has grown very slowly over the years. In that plot, we show the temporal evolution of the cumulative frequency of these stars, starting from the first quantitative abundance analysis reported in the literature (Snedden & Bond 1976). In recent years, Ba dwarfs have been found in the studies of Kong et al. (2018), Purandardas et al. (2019), Shejeelammal et al. (2020), Liu et al. (2021), and Karinkuzhi et al. (2021). We refer the reader to Kong et al. (2018, and references therein) for a complete list until that year.

Recently, based on the Large Sky Area Multi-Object Fiber Spectroscopic Telescope data along with machine-learning techniques, Norfolk et al. (2019) were able to select a sample of 895 *s*-process-rich candidates, using absorption features of Ba II and Sr II in their spectra. These stars were classified into three groups: those with only Ba enhancement (Ba only), only Sr enhancement (Sr only), and both Ba and Sr enhancements (Ba and Sr). However, the Ba only index turned out to be more reliable proxy for identifying potential Ba star candidates (see Karinkuzhi et al. 2021; Guo et al. 2023). As an exercise, we searched for Ba dwarf candidates in the sample of Norfolk et al. (2019), and found 29 stars with superficial gravities such that $\log g \geq 3.5$; among them, only 3 stars are marked as Ba only, according the algorithm employed by these authors. This represents a very low frequency of occurrence (only $\sim 0.3\%$). In the bottom panel of Figure 1, we show the distribution of the sample analyzed by Norfolk et al. That exercise illustrates that the task of finding Ba dwarfs is not easy, which reinforces the need of identifying new candidates and exploring their chemical patterns.

In the present work, we conduct a high-resolution spectroscopic analysis of two potential Ba dwarf candidates, HD 15096 and HD 37792. In addition to them, we have also included in our analysis the star HD 141804, previously classified as CH subgiants by Luck & Bond (1991), and a well-studied Ba dwarf (HD 207585). In the following, we describe in Section 2 the criteria adopted in the selection of the targets, as well as the details of the observation and data acquisition; in Section 3, we give details of the spectroscopic analysis applied to the four stars; in Section 4, we describe the procedure to derive the elemental abundances; in Section 5, we discuss the abundance results in the literature context. In Section 6, we compare the observed patterns for the neutron-capture elements with predictions from the *s*-process nucleosynthesis models. In Section 7, we carry out a kinematic study for the program stars. Concluding remarks are outlined in Section 8.

2. Program Stars and Observations

Fulbright (2000) conducted a high-resolution spectroscopic analysis of 168 halo and disk stars, mainly dwarfs. Among them, we noticed that HD 15096 and HD 37792 stood out of the data set, showing relatively high barium abundances, with $[\text{Ba}/\text{Fe}]^4$ ratios of +0.96 and +1.29 dex, respectively. Such high values caught our attention to consider these two targets as chemically peculiar candidates. Additionally, we realized that the barium abundance of HD 15096 is also accompanied by similar values for the $[\text{Y}/\text{Fe}]$ and $[\text{Zr}/\text{Fe}]$ ratios. However, no other neutron-capture element abundance data were reported for HD 15096 and HD 37792 in the literature.

The stars HD 141804 and HD 207585, in turn, belong to Table 3 of Luck & Bond (1991). That table lists 15 *s*-process enhanced stars with surface gravities ($\log g$) ranging from 3.0 to ~ 4.0 , so labeled as CH subgiants. Later works realized that some of these stars have different $\log g$ values, which put them in other evolutionary stages. This is the case of the stars BD +09°2384, CPD−62°6195 (=CD−62°1346), HD 122202, HD 123585, and HD 207585. For BD+09°2384 and CPD−62°6195, de Castro et al. (2016) and Pereira et al. (2012) found $\log g < 3.0$, which evidenced the giant nature of these

⁴ Throughout this paper, we use the standard spectroscopic notation, $[A/B] = \log(N_A/N_B)_* - \log(N_A/N_B)_\odot$, and the definition $\log \epsilon(A) = \log(N_A/N_H) + 12$.

Table 1
General Description of Our Sample

Star	R.A. (h m s)	Decl. (° ′ ″)	<i>V</i> (mag)	<i>B</i> (mag)	pmRA (mas yr ⁻¹)	pmDEC (mas yr ⁻¹)	Plx (mas)	Date Obs. (yyyy-mm-dd)	Exp. (s)
HD 15096	02 26 01.76	+05 46 46.35	7.930	8.745	+383.857	+162.084	34.1998	2016-09-25	600
HD 37792	05 40 17.43	-19 13 37.77	7.722	8.093	-127.539	-192.658	13.3559	2016-09-09	600
HD 141804	15 53 29.24	-54 09 30.50	9.038	9.582	-21.448	-66.878	11.3044	2016-03-13	900
HD 207585	21 50 34.71	-24 11 11.69	9.785	10.482	+14.390	-36.805	4.8441	2008-10-19	1 200

stars. For HD 122202, HD 123585, and HD 207585, investigations carried out by North et al. (1994), Allen & Barbuy (2006a), Karinkuzhi & Goswami (2015), and Shejeelammal et al. (2020) reported $\log g$ values greater than those reported by Luck & Bond, thus evidencing the dwarf nature of these objects.

For HD 141804, there is no other analysis in addition to that performed by Luck & Bond (1991). For this target, we present here for the first time elemental abundances of nitrogen, oxygen, aluminum, strontium, samarium, europium, and lead, as well as estimates of neutron exposure and a kinematic analysis. For HD 207585, on the other side, Shejeelammal et al. (2020) provided detailed elemental abundances and recognized the Ba dwarf nature of this object. However, as we will demonstrate later, we have found significant differences regarding the nitrogen and oxygen abundances reported by these authors. Additionally, we derived for the first time strontium abundances and estimated the neutron exposure level for HD 207585.

The high-resolution spectra of the program stars were acquired using the Fiber-fed Extended Range Optical Spectrograph (FEROS; Kaufer et al. 1999), installed at the 2.2 m Max Planck Gesellschaft/European Southern Observatory Telescope in La Silla, Chile. The observational missions were carried out between 2008 October and 2016 March. FEROS covers the spectral region between 3500 and 9200 Å with a resolving power $R = \lambda/\Delta\lambda \approx 48,000$. In order to achieve a typical signal-to-noise ratio (S/N) of ≈ 150 –200, the exposure time ranges from 600 to 1200 s. We have used the FEROS Data Reduction System pipeline to reduce the observed spectra. General information about our targets is presented in Table 1, where we provided their positions, proper motions and parallaxes (Gaia Collaboration 2020), V and B magnitudes (Zacharias et al. 2004), observation dates, and corresponding exposure times.

3. Atmospheric and Physical Parameters

The atmospheric parameters, effective temperature (T_{eff}), $\log g$, microturbulent velocity (ξ), and metallicity ($[\text{Fe}/\text{H}]$), for the stars HD 15096, HD 37792, HD 141804, and HD 207585 were derived by applying the same procedure described, for example, in Roriz et al. (2017), Pereira et al. (2019), and Holanda et al. (2020, 2023). First, we measured the equivalent widths (EWs) of a set of Fe I and Fe II absorption lines, by fitting Gaussian profiles to them. For this assignment, we have used the task SPLOT of the IRAF (Tody 1986). The atomic parameters of the Fe I and Fe II transitions, such as excitation potential (χ) and $\log gf$ values, were taken from Lambert et al. (1996), i.e., the same line list consistently employed in the aforementioned references. The EW measurements are listed in Table 10. In the task of deriving the atmospheric parameters, we implemented version 2013 of the MOOG⁵ spectral analysis

code (Snedden 1973; Snedden et al. 2012). MOOG assumes the local thermodynamic equilibrium (LTE) conditions and the plane-parallel atmosphere models. We have adopted the models computed by Kurucz (1993).

To find the effective temperature, we assumed the excitation equilibrium. Such a condition is verified when there is no trend between the iron abundances and the lower excitation potential of the measured Fe I lines, or when the slope of the linear fit is very close to zero. We derived the microturbulent velocity by constraining the Fe I lines until the iron abundance obtained from them showed no dependence on the reduced EW ($\log \text{EW}/\lambda$). The surface gravity is computed by imposing the ionization equilibrium, i.e., when the Fe I and Fe II abundances are equal at the fixed T_{eff} .

The errors associated with temperatures were estimated considering the uncertainty in the value of the slope of the linear fit for Fe I abundances versus χ . On the other hand, the errors associated with microturbulent velocities were estimated from the uncertainty in the slope of the linear fit for the same Fe I abundances versus $\log \text{EW}/\lambda$. The errors in surface gravities were estimated by changing the $\log g$ value until the difference in the average abundances of Fe I and Fe II is equal to the standard deviation of the $[\text{Fe I}/\text{H}]$ mean. The final metallicity was normalized to the solar iron abundance recommendation of Grevesse & Sauval (1998), $\log \epsilon(\text{Fe}) = 7.50$ dex.

Table 2 presents the atmospheric parameters derived in this work and their respective uncertainties, along with data compiled from the literature. In general, we found a good agreement between our results and those reported in previous studies. Furthermore, Table 2 also lists the $\log g$ values derived from GAIA’s parallaxes (Gaia Collaboration 2020); these data corroborate the consistency of our results. In particular, for HD 141804, we derived $\log g = 4.50$, whereas Luck & Bond (1991) reported $\log g = 3.50$, which leads us to conclude that HD 141804 is, in fact, a dwarf star. Regarding HD 207585, we remark the close agreement between the atmospheric parameters derived in this work with those reported recently by Shejeelammal et al. (2020). It is also worth noting that these $\log g$ values are slightly larger than the value derived by Luck & Bond.

To estimate the masses and ages of our targets, we have used the PARSEC (PAдова and TRieste Stellar Evolution Code; Bressan et al. 2012) evolutionary tracks and a Bayesian estimation method (da Silva et al. 2006). This estimation has been performed through PARAM,⁶ a helpful tool to determine the basic intrinsic parameters of stars, given from their photometric and spectroscopic data. Individual values for masses and their respective uncertainties are also listed in Table 2. Additionally, the ages (in Gyr) derived from that procedure are 6.177 ± 3.623 (HD 15096), 4.768 ± 0.556 (HD 37792), 4.241 ± 1.729 (HD 141804), and 5.858 ± 0.561 (HD 207585). The positions of these stars in the Kiel Diagram

⁵ Available at <https://www.as.utexas.edu/chris/moog.html>.

⁶ Available online at http://stev.oapd.inaf.it/cgi-bin/param_1.3.

Table 2
Adopted Atmospheric and Physical Parameters for HD 37792, HD 15096, HD 141804, and HD 207585, in Comparison with Values Previously Reported in the Literature

Star	T_{eff} (K)	$\log g$ (cm s^{-2})	[Fe/H] (dex)	ξ (km s^{-1})	$\log g^{\text{GAIA}}$ (cm s^{-2})	Mass (M_{\odot})	References
HD 15096	5380 ± 30	4.40 ± 0.10	-0.14 ± 0.06	0.80 ± 0.10	4.51 ± 0.02	0.85 ± 0.03	This Work
	5375	4.30	-0.20	0.80	Fulbright (2000)
	5119	4.39	-0.48	0.43	Gratton et al. (2003)
	5247	4.35	-0.41	Soubiran & Girard (2005)
HD 37792	6500 ± 20	4.10 ± 0.20	-0.55 ± 0.09	1.50 ± 0.10	4.09 ± 0.03	1.07 ± 0.04	This Work
	6500	4.10	-0.60	1.50	Fulbright (2000)
HD 141804	6230 ± 50	4.50 ± 0.10	-0.41 ± 0.08	1.20 ± 0.10	4.35 ± 0.03	0.99 ± 0.04	This Work
	6000	3.50	-0.41	1.70	Luck & Bond (1991)
HD 207585	5840 ± 50	3.90 ± 0.20	-0.34 ± 0.08	1.10 ± 0.10	3.84 ± 0.03	1.10 ± 0.04	This Work
	5400	3.50	-0.74	Smith & Lambert (1986)
	5400 ± 300	3.30 ± 0.30	-0.57 ± 0.05	1.80 ± 0.50	Luck & Bond (1991)
	5800 ± 100	3.80 ± 0.20	-0.38 ± 0.12	1.00 ± 0.20	Shejeelammal et al. (2020)

are shown in Figure 2, along with evolutionary tracks for metallicities $Z = 0.006, 0.008,$ and 0.014 . From this plot, we see that at least HD 207585 is in a post-main-sequence evolutionary stage.

Since effective temperatures, surface gravities, and stellar masses have been derived for the program stars, we can evaluate their luminosities from the relation:

$$\log\left(\frac{L_{\star}}{L_{\odot}}\right) = 4 \log T_{\text{eff}\star} - \log g_{\star} + \log\left(\frac{M_{\star}}{M_{\odot}}\right) - 10.61, \quad (1)$$

for which we adopted $T_{\text{eff}\odot} = 5777$ K and $\log g_{\odot} = 4.44$. By inserting the data provided in Table 2 into Equation (1), we found $\log(L_{\star}/L_{\odot}) = -0.16 \pm 0.10, +0.57 \pm 0.20, +0.06 \pm 0.10,$ and $+0.60 \pm 0.20$, for HD 15096, HD 37792, HD 141804, and HD 207585, respectively.

We can also derive their luminosities based on parallaxes, from the relation:

$$\log\left(\frac{L_{\star}}{L_{\odot}}\right) = -2 \log \pi + 0.4(M_{\text{bol}\odot} - V + A_V - \text{BC} - 5), \quad (2)$$

where π is the parallax (in arcseconds), $M_{\text{bol}\odot} = 4.740 \pm 0.024$ is the solar bolometric magnitude of Bessell et al. (1998), V is the visual magnitude, BC is the bolometric correction, and A_V is the interstellar extinction. The bolometric corrections were evaluated from the empirical calibrations provided by Alonso et al. (1995) for dwarf stars, whereas the A_V values were estimated from the empirical extinction law of Chen et al. (1998). From this procedure, we have estimated $\log(L_{\star}/L_{\odot}) = -0.31 \pm 0.04, +0.63 \pm 0.05, +0.28 \pm 0.06,$ and $+0.65 \pm 0.05$, for HD 15096, HD 37792, HD 141804, and HD 207585, respectively.

3.1. Radial Velocity Data

As will be discussed in Section 5, the chemical peculiarities observed in our stars cannot be explained in light of the stellar evolution of an isolated star, but in the mass-transfer framework. Hence, in this section, we discuss the binary status of our targets. According to the SIMBAD database, they are all classified as spectroscopic binaries. Three of them, HD 15096,

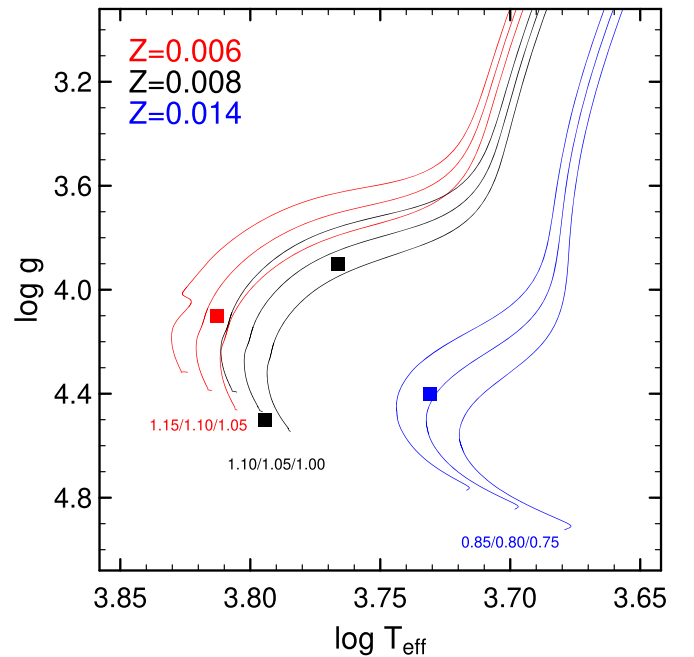


Figure 2. Position of the stars HD 15096 (blue), HD 37792 (red), HD 141804 (black), and HD 207585 (black) in the $\log T_{\text{eff}}$ vs. $\log g$ diagram. Evolutionary tracks from Bressan et al. (2012), for $Z = 0.006, 0.008,$ and 0.014 , are also shown; the numbers correspond to stellar masses (in solar mass units, M_{\odot}).

HD 141804, and HD 207585, have their orbital elements already determined, and made available in the ninth catalog of spectroscopic binary orbits (the SB9⁷ database; Pourbaix et al. 2004). HD 15096, HD 141804, and HD 207585 exhibit circular orbits (i.e., $e \sim 0.0$) with orbital periods (in days) of $3600 \pm 41, 2652 \pm 95,$ and 672 ± 2 , respectively (Latham et al. 2002; Escorza et al. 2019). As binary systems, their chemical peculiarities are attributable to mass transfer. We have also derived their radial velocities, from the Doppler shift of the spectral lines. We obtained, in kilometers per second, $-5.625 \pm 0.194, +10.133 \pm 0.440, -55.301 \pm 0.406,$ and -55.891 ± 0.309 for HD 15096, HD 37792, HD 141804, and HD 207585, respectively.

⁷ Available online at <https://sb9.astro.ulb.ac.be/>.

Table 3
Elemental Abundances Derived for the Stars HD 15096 and HD 37792

Species	log ϵ_{\odot}	HD 15096					HD 37792				
		log ϵ	σ_{obs}	$n(\#)$	[X/H]	[X/Fe]	log ϵ	σ_{obs}	$n(\#)$	[X/H]	[X/Fe]
C I	8.52	8.67	0.09	03	+0.15	+0.29	8.43	0.10	11	-0.09	+0.46
C(C ₂ 5165)	8.52	8.70	0.02	syn	+0.18	+0.32
C(C ₂ 5635)	8.52	8.65	0.03	syn	+0.13	+0.27
N	7.92	8.07	0.10	syn	+0.15	+0.29
O I	8.83	8.83	0.33	syn	0.00	+0.14	8.55*	0.04	03	-0.28	+0.27
Na I	6.33	6.18	0.06	04	-0.15	-0.01	5.97	0.05	04	-0.36	+0.19
Mg I	7.58	7.58	0.10	05	0.00	+0.14	7.18	0.10	07	-0.40	+0.15
Al I	6.47	6.24	0.05	06	-0.23	-0.09
Si I	7.55	7.51	0.04	05	-0.04	+0.10	7.17	0.07	05	-0.38	+0.17
Ca I	6.36	6.22	0.08	10	-0.14	0.00	5.93	0.09	15	-0.43	+0.12
Ti I	5.02	4.79	0.09	20	-0.23	-0.09	4.42	0.08	14	-0.60	-0.05
Cr I	5.67	5.44	0.06	05	-0.23	-0.09	5.02	0.07	08	-0.65	-0.10
Fe I	7.50	7.36	0.06	89	-0.14	...	6.95	0.09	74	-0.55	...
Fe II	7.50	7.35	0.05	14	-0.15	...	6.95	0.07	12	-0.55	...
Ni I	6.25	6.05	0.08	21	-0.20	-0.06	5.85	0.11	07	-0.40	+0.15
Sr I	2.97	3.70	0.04	01	+0.73	+0.87	3.04	0.07	01	+0.07	+0.62
Y II	2.24	3.07	0.07	05	+0.83	+0.97	2.54	0.09	06	+0.30	+0.85
Zr II	2.60	3.51	0.14	04	+0.91	+1.05	2.98	0.11	04	+0.38	+0.93
Ba II	2.13	3.13	0.06	syn	+1.00	+1.14	3.03	0.10	syn	+0.90	+1.45
La II	1.17	1.96	0.11	05	+0.79	+0.93	1.59	0.09	03	+0.42	+0.97
Ce II	1.58	2.47	0.10	07	+0.89	+1.03	2.05	0.08	06	+0.47	+1.02
Nd II	1.50	2.25	0.05	07	+0.75	+0.89	1.93	0.11	07	+0.43	+0.98
Sm II	1.01	1.68	0.03	04	+0.67	+0.81	1.78	...	02	+0.77	+1.32
Eu II	0.51	0.71	0.09	syn	+0.20	+0.34
Pb I	1.95	2.85	0.10	syn	+0.90	+1.04	<1.90	...	syn	< -0.05	< +0.50
C	8.52	8.67	0.03	03	+0.15	+0.29

Note. For guidance, the solar photospheric abundances adopted in this work (Grevesse & Sauval 1998) are listed in the second column. The third and eighth columns provide the stellar abundances in the scale log $\epsilon(\text{H}) = 12.0$; an asterisk is used to indicate abundances with non-LTE corrections. Abundances in the [X/H] and [X/Fe] notations are also shown. In columns (4) and (9), we provide the abundance dispersion (σ_{obs}) due to line-to-line scatter. These were evaluated when three or more transitions were considered, except for strontium and elements whose abundances were derived from spectral synthesis (syn), as explained in the text. For abundances based on EW measurements, we provide information on the number of spectral lines used. In the end, we give the mean carbon abundance, considering the abundances derived from atomic absorption lines and the synthesis of molecular bands with the respective dispersion. In this case, $n(\#)$ is the number of abundances obtained.

4. Abundance Analysis

Chemical abundances were derived for a set of 21 different elements, based on either EW measurements or synthetic spectra computations of selected absorption lines. To carry out this task, we have used the drivers *abfind*, *blends*, and *synth* of MOOG. The final abundances are presented in Tables 3 and 4, and a comparison with literature values is provided in Table 5. Our abundance data are normalized to the solar value recommended by Grevesse & Sauval (1998).

Carbon abundances were determined from EW measurements of some absorption atomic lines of C I and also by computing synthetic spectra of molecular band heads for the stars HD 15096, HD 141804, and HD 207585. For HD 37792, the warmer (6500 K) star of the program, the carbon molecular features were present for carbon abundance determination. Therefore, the carbon abundance for this object was estimated only based on the C I atomic lines present in its spectrum, as seen in Table 3. To synthesize the molecular carbon features observed in HD 15096, HD 141804, and HD 207585, we used the C₂ (0,0) band head of the Swan system $d^3\Pi_g - a^3\Pi_u$ at 5165 Å, as performed in Roriz et al. (2017), and the C₂ (0,1) band head of the Swan system $d^3\Pi_g - a^3\Pi_u$ at 5635 Å, as in Drake & Pereira (2008). Figure 3 shows the observed and

synthetic spectra around the spectral region of the C₂ molecular band at 5635 Å, for these stars.

Nitrogen abundances were also obtained via the spectral synthesis technique. For HD 15096, we used the ¹²CN molecular lines of the system $A^2\Pi - X^2\Sigma$ in the 7994–8020 Å wavelength range, adopting the same line list provided in Drake & Pereira (2008). For the stars HD 141804 and HD 207585, we used the $B^2\Sigma - X^2\Sigma$ violet system band head at 3883 Å, as done in Roriz et al. (2017), with the line list provided by the Vienna Atomic Line Database (VALD; Ryabchikova et al. 2015). For HD 37792, however, we were not able to derive its nitrogen abundance. Additionally, the carbon isotopic ratios, ¹²C/¹³C, could not be measured in our program stars, as they are too hot to identify the ¹³CN lines. It is also worth mentioning that nitrogen abundances in Ba dwarfs are reported in the literature for a very limited number of stars (Reddy et al. 2003; Allen & Barbuy 2006a; Drake & Pereira 2007; Purandardas et al. 2019; Shejeelammal et al. 2020; Liu et al. 2021). Among them, many values are upper limits for the [N/Fe] ratios.

Concerning oxygen abundances, we have used the [O I] forbidden line at 6300.3 Å for the star HD 15096 and adopted log $gf = -9.72$ from Allende Prieto et al. (2001). For HD 37792, HD 141804, and HD 207585, oxygen abundances

Table 4
Same as in Table 3, for the Stars HD 141804 and HD 207585

Species	$\log \epsilon_{\odot}$	HD 141804					HD 207585				
		$\log \epsilon$	σ_{obs}	$n(\#)$	[X/H]	[X/Fe]	$\log \epsilon$	σ_{obs}	$n(\#)$	[X/H]	[X/Fe]
C I	8.52	8.85	0.08	09	+0.33	+0.74	8.97	0.09	09	+0.45	+0.79
C(C ₂ 5165)	8.52	8.72	0.03	syn	+0.20	+0.61	8.72	0.03	syn	+0.20	+0.54
C(C ₂ 5635)	8.52	8.62	0.10	syn	+0.10	+0.51	8.82	0.03	syn	+0.30	+0.64
N	7.92	7.62	0.03	syn	-0.30	+0.11	7.52	0.04	syn	-0.40	-0.06
O I	8.83	8.58*	0.04	03	-0.25	+0.16	8.55*	0.10	03	-0.28	+0.06
Na I	6.33	6.06	0.06	04	-0.27	+0.14	6.18	0.10	04	-0.15	+0.19
Mg I	7.58	7.29	0.12	04	-0.29	+0.12	7.33	0.06	03	-0.25	+0.09
Al I	6.47	5.96	0.07	03	-0.51	-0.10	5.96	0.07	04	-0.51	-0.17
Si I	7.55	7.32	0.04	03	-0.23	+0.18	7.39	0.07	03	-0.16	+0.18
Ca I	6.36	6.01	0.07	16	-0.35	+0.06	6.09	0.09	17	-0.27	+0.07
Ti I	5.02	4.54	0.06	16	-0.48	-0.07	4.56	0.08	18	-0.46	-0.12
Cr I	5.67	5.22	0.07	08	-0.45	-0.04	5.30	0.10	05	-0.37	-0.03
Fe I	7.50	7.09	0.08	64	-0.41	...	7.16	0.08	73	-0.34	...
Fe II	7.50	7.10	0.07	12	-0.40	...	7.16	0.08	11	-0.34	...
Ni I	6.25	5.92	0.08	10	-0.33	+0.08	5.96	0.09	09	-0.29	+0.05
Sr I	2.97	3.81	0.07	01	+0.84	+1.25	3.88	0.07	01	+0.91	+1.25
Y II	2.24	3.18	0.05	06	+0.94	+1.35	3.24	0.10	06	+1.00	+1.34
Zr II	2.60	3.67	0.11	07	+1.07	+1.48	3.78	0.11	06	+1.18	+1.52
Ba II	2.13	3.43	0.06	syn	+1.30	+1.71	3.53	0.02	syn	+1.40	+1.74
La II	1.17	2.29	0.05	05	+1.12	+1.53	2.21	0.09	05	+1.04	+1.38
Ce II	1.58	2.86	0.09	12	+1.28	+1.69	2.84	0.09	06	+1.26	+1.60
Nd II	1.50	2.68	0.08	14	+1.18	+1.59	2.61	0.06	10	+1.11	+1.45
Sm II	1.01	1.94	0.07	06	+0.93	+1.34	1.88	0.07	07	+0.87	+1.21
Eu II	0.51	0.88	0.05	syn	+0.37	+0.78	0.76	0.04	syn	+0.25	+0.59
Pb I	1.95	3.00	0.13	syn	+1.05	+1.46	2.96	0.10	syn	+1.01	+1.35
C	8.52	8.73	0.12	03	+0.21	+0.62	8.84	0.13	03	+0.32	+0.66

Table 5

Comparison between Elemental Abundances Derived in (1) This Work, (2) Fulbright (2000), (3) Luck & Bond (1991), (4) Shejeelammal et al. (2020), and (5) Masseron et al. (2010)

Star	[C/Fe]	[N/Fe]	[O/Fe]	[Na/Fe]	[Mg/Fe]	[Al/Fe]	[Si/Fe]	[Ca/Fe]	[Ti/Fe]	[Cr/Fe]	References
HD 15096	+0.29	+0.29	+0.14	-0.01	+0.14	-0.09	+0.10	0.00	-0.09	-0.09	(1)
...	+0.04	+0.21	+0.19	+0.08	+0.09	+0.13	-0.01	(2)
HD 37792	+0.46	...	+0.27	+0.19	+0.15	...	+0.17	+0.17	-0.05	-0.10	(1)
...	+0.13	+0.11	...	+0.31	+0.15	+0.33	...	(2)
HD 141804	+0.62	+0.11	+0.16	+0.14	+0.12	-0.10	+0.18	+0.06	-0.07	-0.04	(1)
...	+0.24	+0.01	-0.08	...	+0.14	+0.15	+0.32	-0.03	(3)
HD 207585	+0.66	-0.06	+0.06	+0.19	+0.09	-0.17	+0.18	+0.07	-0.12	-0.03	(1)
...	+0.25	+0.02	...	+0.28	+0.39	+0.01	+0.24	(3)
...	+0.61	+0.75	+0.97	+0.25	+0.07	...	+0.12	+0.26	+0.01	+0.13	(4)
...	+0.51	+0.12	+0.14	...	-0.03	(5)
Star	[Ni/Fe]	[Y/Fe]	[Zr/Fe]	[Ba/Fe]	[La/Fe]	[Ce/Fe]	[Nd/Fe]	[Sm/Fe]	[Eu/Fe]	[Pb/Fe]	References
HD 15096	-0.06	+0.97	+1.05	+1.14	+0.93	+1.03	+0.89	+0.81	+0.34	+1.04	(1)
...	0.00	+1.02	+1.00	+0.96	+0.30	...	(2)
HD 37792	+0.15	+0.85	+0.93	+1.45	+0.97	+1.02	+0.98	+1.32	...	+0.50	(1)
...	+0.10	+1.29	(2)
HD 141804	+0.08	+1.35	+1.48	+1.71	+1.53	+1.69	+1.59	+1.34	+0.78	+1.46	(1)
...	+0.02	+0.60	+1.48	+1.25	+1.18	+1.10	+0.95	(3)
HD 207585	+0.05	+1.34	+1.52	+1.74	+1.38	+1.60	+1.45	+1.21	+0.59	+1.35	(1)
...	+0.08	+1.30	+1.02	...	+1.61	+0.85	+0.94	+1.06	(2)
...	-0.01	+1.37	+1.20	+1.60	+1.70	+1.72	+1.62	+2.04	+0.28	...	(3)
...	+1.23	+1.37	+1.41	+0.58	+1.30	(4)

were evaluated from the EW measurements of the oxygen infrared triplet around 7774 Å. Accounting for the well-known non-LTE effects in the oxygen infrared triplet lines, we performed non-LTE corrections for abundances derived from the OI triplet lines. For this, we used yields of Amarsi et al.

(2015), which are available by the INSPECT database, version 1.0⁸. After the non-LTE corrections, the [O/Fe] ratios for HD 141804 and HD 207585 were lowered by 0.22 and

⁸ Available at <http://www.inspect-stars.com/>.

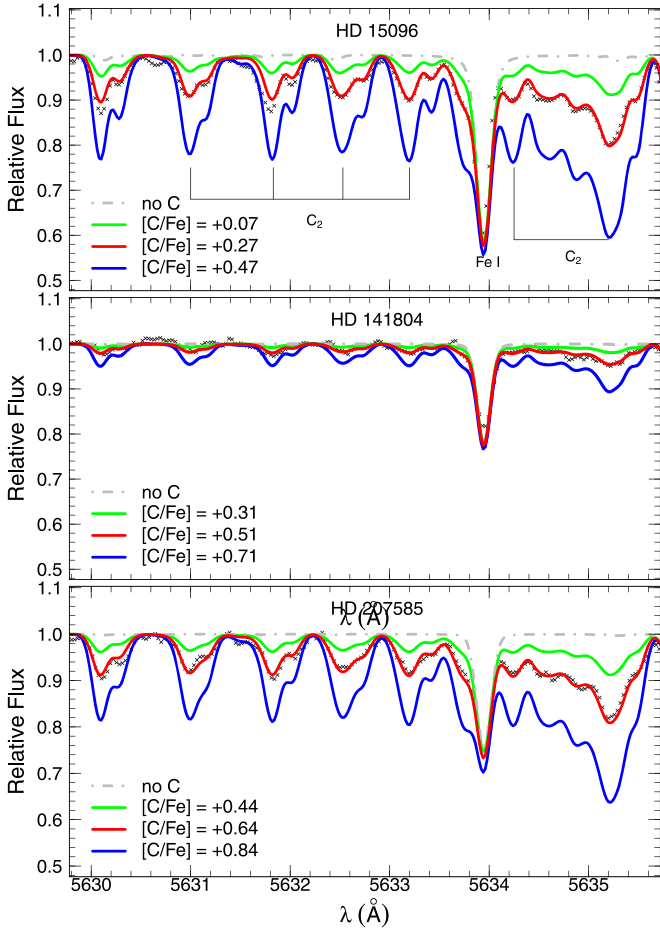


Figure 3. Observed (crosses) and synthetic (lines) spectra around the spectral region of the C_2 molecular band at 5635 Å for the stars HD 15096, HD 141804, and HD 207585. The synthetic spectra were computed for different $[C/Fe]$ values, as indicated in each panel. The gray lines are spectral synthesis without the contribution of the C_2 molecule.

0.31 dex, respectively, while for HD 15096 the corrected $[O/Fe]$ ratio increased in 0.02 dex. The adopted values are marked with an asterisk in Tables 3 and 4.

For the light elements Na, Mg, Al, Si, Ca, and Ti, the iron-group elements Cr and Ni, and the neutron-capture elements Sr, Y, Zr, La, Ce, Nd, and Sm, abundances were derived from EW measurements of selected atomic lines sufficiently unblended to provide reliable abundances of such species. In Table 11 of the Appendix, we provide the adopted lab data, such as wavelength, excitation potentials, and $\log gf$ values, of the atomic transitions used in our analysis, as well as the measured EWs. For the element lanthanum, in particular, we have followed the same procedure employed by Roriz et al. (2021b). In other words, we measured the EWs of the lanthanum lines and run driver *blends* of MOOG, which provides abundances from blended spectral lines, to account for the hyperfine splitting (HFS) that strongly affect the transitions of this element.

Barium, europium, and lead abundances, on the other hand, were determined from synthetic spectrum analysis. For barium abundances, we used the Ba II line at 5853.7 Å and adopted its HFS data from McWilliam (1998). For europium, we considered the Eu II line at 6645.1 Å, for which HFS components were taken from Lawler et al. (2001b). Lead abundances were derived from the Pb I line at 4057.8 Å. HFS and isotopic data for lead were taken from Van Eck et al. (2003).

4.1. Abundance Uncertainties

In the task of deriving chemical abundances, two uncertainty sources should be taken into account: (i) the line parameters, as EW measurements, oscillator strength values, continuum normalization, and line blending, which introduce random errors (σ_{ran}) in abundances, as well as (ii) the errors associated with stellar parameters of atmospheric models. For a generic element X, the total uncertainty in $\log \epsilon(X)$ can be evaluated according to the following equation:

$$\begin{aligned} \sigma_{\log \epsilon(X)_*}^2 = & \sigma_{\text{ran}}^2 + \left(\frac{\partial \log \epsilon}{\partial T_{\text{eff}}} \right)^2 \sigma_{T_{\text{eff}}}^2 \\ & + \left(\frac{\partial \log \epsilon}{\partial \log g} \right)^2 \sigma_{\log g}^2 + \left(\frac{\partial \log \epsilon}{\partial \xi} \right)^2 \sigma_{\xi}^2 \\ & + \left(\frac{\partial \log \epsilon}{\partial [Fe/H]} \right)^2 \sigma_{[Fe/H]}^2 + \left(\frac{\partial \log \epsilon}{\partial W_{\lambda}} \right)^2 \sigma_{W_{\lambda}}^2. \quad (3) \end{aligned}$$

To evaluate the partial derivatives of the above equation, we shifted the parameters T_{eff} , $\log g$, ξ , $[Fe/H]$, and W_{λ} in +30 K, +0.1 dex, +0.1 km s^{-1} , +0.1 dex, and +3 mÅ, respectively, which are typical uncertainties. Then, we computed the corresponding change introduced in the abundance when we varied one of the parameters, keeping the others fixed. For a resolution $R = 48,000$ and a typical S/N of $\sim 100\text{--}200$, the expected uncertainties in the EWs are on the order of 2–3 mÅ, according to de Strobel & Spite (1988). The σ_{ran} term in Equation (3) takes the line-to-line scatter in abundance into account. It is evaluated as the ratio $\sigma_{\text{obs}}/\sqrt{n}$, where σ_{obs} is the standard deviation and n is the number of spectral lines considered in the abundance derivation. Thus, the uncertainty in the $[X/Fe]$ ratios is given by:

$$\sigma_{[X/Fe]}^2 = \sigma_X^2 + \sigma_{Fe}^2. \quad (4)$$

The partial derivatives in Equation (3) were evaluated for HD 15096, taken as a template star. Table 6 shows the abundances for HD 15096 change in response to changes in T_{eff} , $\log g$, ξ , $[Fe/H]$, and W_{λ} ; these values were assumed for the other targets. On the other hand, σ_{ran} was computed for each object, when three or more lines are used to derive abundances, except for strontium and elements whose abundances were derived from spectral synthesis. For these particular cases, σ_{obs} is evaluated from three different positions of the continuum.

For CNO abundances, the uncertainties were evaluated similarly. By varying one of the parameters T_{eff} , $\log g$, and ξ , keeping the other two constant, we computed the respective changes introduced in abundances of HD 15096. Additionally, since CNO abundances are not independent of each other, we also evaluated the variations introduced as a consequence of changes in $\log \epsilon(C)$, $\log \epsilon(N)$, and $\log \epsilon(O)$ individually. The results for the CNO uncertainty estimates are presented in Table 7.

5. Results and Discussion

5.1. Carbon, Nitrogen, and Oxygen

Elemental abundances of carbon, nitrogen, and oxygen are sensitive indexes to stellar evolution stages, as well as the mixing events that take place within the stars and alter the chemical composition of their atmospheres. According to

Table 6
Abundance Uncertainties for HD 15096, Taken as a Template Star

Species	σ_{ran}	ΔT_{eff} (+30 K)	$\Delta \log g$ (+0.1 dex)	$\Delta \xi$ (+0.1 km s ⁻¹)	$\Delta[\text{Fe}/\text{H}]$ (-0.1 dex)	ΔW_{λ_i} (+3 mÅ)	$\sqrt{\sum \sigma^2}$	σ_{obs}
C I	0.05	-0.02	+0.01	0.00	0.00	+0.08	0.10	0.09 (03)
Na I	0.03	+0.02	-0.02	-0.01	-0.01	+0.04	0.06	0.06 (04)
Mg I	0.04	+0.02	-0.01	-0.01	-0.01	+0.04	0.06	0.10 (05)
Al I	0.02	+0.02	-0.01	0.00	0.00	+0.05	0.06	0.05 (06)
Si I	0.02	-0.01	0.00	-0.01	-0.02	+0.05	0.06	0.04 (05)
Ca I	0.03	+0.03	-0.02	-0.02	-0.01	+0.05	0.07	0.08 (10)
Ti I	0.03	+0.04	0.00	-0.02	0.00	+0.07	0.09	0.09 (20)
Cr I	0.03	+0.04	-0.01	-0.03	-0.01	+0.06	0.08	0.06 (05)
Fe I	0.01	+0.01	-0.01	-0.03	-0.02	+0.06	0.07	0.06 (89)
Fe II	0.01	-0.02	+0.03	-0.02	-0.03	+0.08	0.10	0.05 (14)
Ni I	0.02	+0.01	+0.01	-0.02	-0.02	+0.07	0.08	0.08 (21)
Sr I	0.02	+0.04	-0.03	-0.03	-0.03	+0.04	0.08	0.04 (01)
Y II	0.03	+0.01	+0.02	-0.04	-0.03	+0.07	0.09	0.07 (05)
Zr II	0.07	0.00	+0.03	-0.04	-0.03	+0.09	0.13	0.14 (04)
Ba II	0.03	0.00	0.00	-0.10	-0.10	...	0.14	0.06 (syn)
La II	0.05	-0.01	+0.02	-0.01	-0.05	+0.07	0.10	0.11 (05)
Ce II	0.04	+0.01	+0.04	-0.03	-0.03	+0.10	0.12	0.10 (07)
Nd II	0.02	+0.01	+0.04	-0.02	-0.04	+0.11	0.13	0.05 (07)
Sm II	0.02	+0.01	+0.04	-0.02	-0.03	+0.11	0.12	0.03 (04)
Eu II	0.05	-0.05	0.00	0.00	-0.05	...	0.09	0.09 (syn)
Pb I	0.06	0.00	0.00	-0.10	-0.10	...	0.15	0.10 (syn)

Note. The second column gives the random errors, given by $\sigma_{\text{ran}} = \sigma_{\text{obs}}/\sqrt{n}$, where n is the number of absorption lines used for the abundance determination. Columns (3) to (7) show variations in the abundances introduced by changes in T_{eff} , $\log g$, ξ , $[\text{Fe}/\text{H}]$, and EW measurements (W_{λ_i}), respectively. By combining quadratically the terms from the second to the seventh columns, we estimate the total uncertainties, listed in column (8). The last column provides the abundance dispersion in abundance due to line-to-line scatter, previously shown in Table 3.

Table 7
Abundance Uncertainties of Carbon, Nitrogen, and Oxygen for the Star HD 15096

Species	ΔT_{eff} (+30 K)	$\Delta \log g$ (+0.1 dex)	$\Delta \xi$ (+0.1 km s ⁻¹)	$\Delta \log(\text{C})$ (+0.20 dex)	$\Delta \log(\text{N})$ (+0.20 dex)	$\Delta \log(\text{O})$ (+0.20 dex)	$\sqrt{\sum \sigma^2}$
C	-0.01	+0.02	-0.01	...	0.00	+0.07	0.07
N	0.00	0.00	-0.02	-0.20	...	-0.14	0.24
O	0.00	+0.05	+0.05	-0.02	0.00	...	0.07

stellar evolution models, when a star becomes a giant, the nuclear material previously exposed to the CN cycle is brought to the stellar surface, as a result of convective motions, known as the first dredge-up (FDU), changing the initial abundance pattern of the star. As an outcome of FDU, carbon is depleted and nitrogen is increased on the stellar surface, while the oxygen content remains unchanged. Unlike the classical Ba/CH stars, Ba dwarfs did not experience the FDU. Consequently, the s -processed material received from their companions is unmixed with the nuclear material internally processed in the star. This is particularly useful for studying carbon and nitrogen, whose abundances should reflect the added material.

In Figure 4, we show the $[\text{C}, \text{N}, \text{O}/\text{Fe}]$ ratios observed for HD 15096, HD 37792, HD 141804, and HD 207585 as functions of the metallicity. We have also added in this figure data compiled from different sources of the literature for dwarf and giant normal stars, classical Ba giants, and Ba dwarf stars (i.e., with $\log g \geq 3.5$). The program stars exhibit moderate levels of carbon enhancements, with $[\text{C}/\text{Fe}]$ ratios ranging from $\sim +0.30$ to $\sim +0.70$ dex, consistent with values already reported in the literature for Ba dwarfs of the same metallicity.

Regarding nitrogen abundances in Ba dwarfs, the scarcity of data in the literature is noteworthy. Among the reported data,

most of them are upper limits (see Allen & Barbuy 2006a) and are not plotted in Figure 4. It is remarked that Ba stars present generally a scatter larger than the observed in normal giant and dwarf stars, and some of them exhibit high levels of N abundances. It is known that massive ($\gtrsim 4.0 M_{\odot}$) TP-AGB stars are able to produce high amounts of nitrogen through the hot bottom burning phenomenon (Boothroyd et al. 1995) when the convective envelope of the AGB star deepens its base into the H-burning shell. In principle, this mechanism could account for the nitrogen excess observed in some Ba stars; however, the patterns observed for heavy elements in Ba stars evidence the low-mass ($\lesssim 3.0 M_{\odot}$) nature of the polluting AGB stars (e.g., Karinkuzhi et al. 2018b; Cseh et al. 2018, 2022; Shejeelammal et al. 2020; Roriz et al. 2021a, 2021b).

For HD 15096, HD 141804, and HD 207585, we have derived $[\text{N}/\text{Fe}] = +0.29, +0.11, \text{ and } -0.06$ dex, respectively. These values are commonly found in normal stars, as seen in the middle panel of Figure 4. This in turn could indicate inefficiencies in the CN cycle and/or FDU of the ancient polluting stars, when they became giants. For HD 37792, our warmest (6500 K) star, N abundance could not be determined. As we mentioned in Section 2, HD 207585 is a common star with the sample of Shejeelammal et al. (2020), who reported

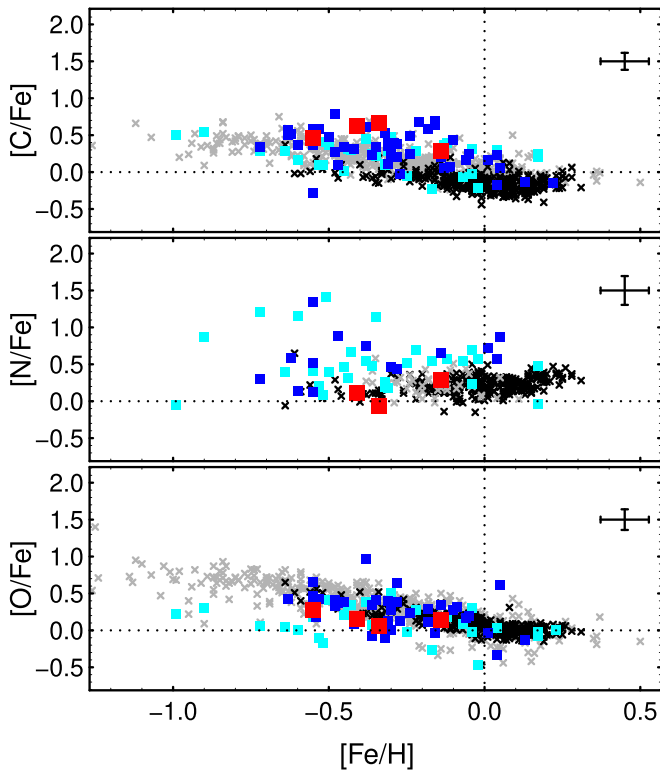


Figure 4. Abundance ratios for the elements carbon, nitrogen, and oxygen. The observed $[C, N, O/Fe]$ ratios for the program stars (red squares) are plotted as functions of the metallicity. Typical error bars are shown at the top of the panels. Data for field dwarf stars (gray crosses), field giant stars (black crosses), Ba giant stars (cyan squares), and Ba dwarf/CH subgiant stars (blue squares), collected from different literature sources, are also plotted. Data for field giant stars were taken from Luck & Heiter (2007); data for field dwarf stars were taken from Reddy et al. (2003), Reddy et al. (2006), and Luck & Heiter (2006); data for Ba giant stars were taken from Allen & Barbuy (2006a), de Castro et al. (2016), Karinkuzhi et al. (2018b), Shejeelammal et al. (2020), and Roriz et al. (2021b); data for Ba dwarfs/CH subgiant stars were taken from Edvardsson et al. (1993), Smith et al. (1993), North et al. (1994), Porto de Mello & da Silva (1997), Pereira & Junqueira (2003), Reddy et al. (2003), Pereira (2005), Allen & Barbuy (2006a), Pereira & Drake (2011), Karinkuzhi & Goswami (2015), Kong et al. (2018), Purandardas et al. (2019), Shejeelammal et al. (2020), Liu et al. (2021), and Karinkuzhi et al. (2021).

$[N/Fe] = +0.75$ dex (see Table 5), while we have found a significantly lower value ($[N/Fe] = -0.06$ dex). For the same object, Masseron et al. (2010) reported $[N/Fe] = +0.12$ dex. Similar disagreement concerns the oxygen abundance of HD 207585. In this work, we found $[N/Fe] = +0.06$ dex, and Masseron et al. (2010) found $[N/Fe] = +0.14$ dex, while Shejeelammal et al. reported a much higher value, $[O/Fe] = +0.97$ dex.

For oxygen, the third panel of Figure 4 shows that our stars follow the Galactic trend, as expected. Additionally, we have derived their respective C/O ratios, which are commonly used to constraint Ba stars ($C/O < 1$; Barbuy et al. 1992; Allen & Barbuy 2006a; Pereira & Drake 2009; Karinkuzhi et al. 2018a, 2018b; Roriz et al. 2023) and CH stars ($C/O > 1$; Pereira & Drake 2009; Pereira et al. 2012; Goswami et al. 2016; Purandardas et al. 2019). For HD 15096, HD 37792, HD 141804, and HD 207585, we found $C/O = 0.69, 0.76, 1.41,$ and 1.95 , respectively.

Considering the CNO abundance data, we can infer that carbon is actually the main responsible for the CNO excess observed in HD 15096, HD 141804, and HD 207585. This is

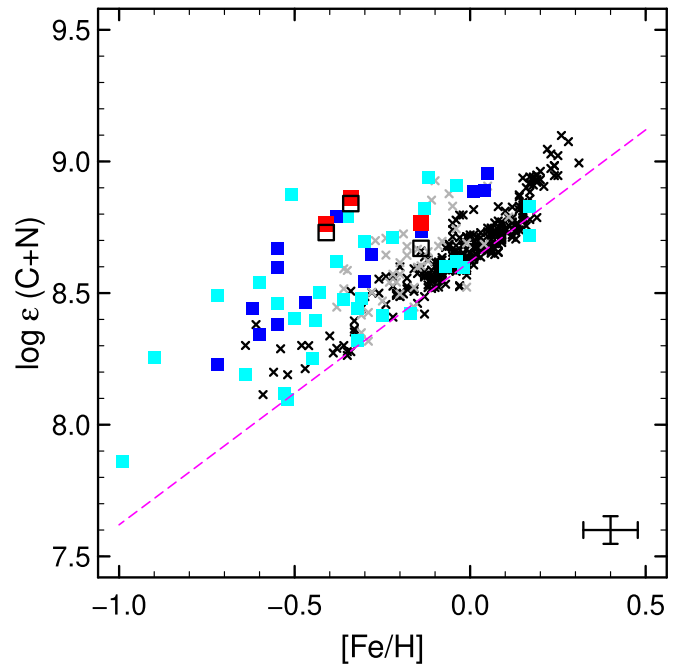


Figure 5. Combined carbon plus nitrogen abundances in the notation $\log \epsilon(C + N)$ observed in HD 15096, HD 141804, and HD 207585 as functions of the metallicity. A typical error bar is also shown. The symbols have the same meaning as in Figure 4. To illustrate the role of carbon in the CNO excess in our stars, we show the respective logarithmic carbon abundances in empty black squares. The magenta dashed line shows the initial CN abundance for a given metallicity.

also seen from their C + N combined abundances, for which we have $\log \epsilon(C + N) = 8.76, 8.76,$ and 8.86 , respectively. In Figure 5, we compare the observed values of $\log \epsilon(C + N)$ with those found in Ba dwarfs, Ba giants, and normal stars. It is notable that Ba stars present in this plane a scatter greater than the observed in normal field stars. Our stars lie close to other Ba dwarfs, which exhibit values systematically larger than those typically found in Ba giants. In conclusion, we see that the atmospheres of our stars were, indeed, contaminated by material previously exposed to the He-burning shell.

5.2. Elements from Sodium to Nickel

We extracted chemical abundances for Na, α -elements (Mg, Al, Si, Ca, and Ti), and iron-group (Cr and Ni) elements. Nucleosynthesis computations performed by Woosley & Weaver (1995) predict that the elements sodium, magnesium, aluminum, silicon, calcium, and titanium in the Galaxy are mainly produced in hydrostatic burning environments of stars with initial masses of $10\text{--}40 M_{\odot}$, as well as in supernova events. Sodium, magnesium, and aluminum are by-products of carbon burning, while most silicon, calcium, and titanium are produced from oxygen burning. Magnesium nucleosynthesis has also a contribution from hydrostatic neon burning. Type II supernova events are able to synthesize silicon and calcium, whereas the elements titanium, iron, chromium, and nickel, belonging to the iron group, are mainly produced from Type Ia supernovae. Therefore, Ba stars are expected to follow the Galactic trend for these elements. According to the data in Tables 3 and 4, the $[X/Fe]$ ratios for elements from Na to Ni are close to zero, similar to values observed in normal field stars.

Table 8Contribution (%) of the s -process to the Solar System Material as Provided by Arlandini et al. (1999, A99) and Bisterzo et al. (2014, B14)

Species	A99	B14
Sr	85	69
Y	92	72
Zr	83	66
Ba	81	85
La	62	76
Ce	77	84
Nd	56	58
Sm	29	31
Eu	6	6
Pb	46	87

In particular, for the odd- Z element Na, the $[\text{Na}/\text{Fe}]$ ratios observed in field stars of the Galaxy show no trend for $[\text{Fe}/\text{H}] \gtrsim -1.0$ dex (e.g., Luck & Heiter 2006, 2007). For the studied stars, we found the $[\text{Na}/\text{Fe}]$ ratios ranging from -0.03 to $+0.19$ dex, consistent with values reported for Ba dwarfs (e.g., Allen & Barbuy 2006a). Na can be produced through the NeNa chain, during the H burning in the convective core of main-sequence stars with masses $M \gtrsim 1.5 M_{\odot}$. Then, when the star becomes a giant, FDU brings Na to the stellar surface, along with the by-products of the CNO cycle. However, since our targets did not reach the giant branch stage of their evolution, their internally processed nuclear material was not dredged yet, so that they behave as normal stars. Works in the literature (Antipova et al. 2004; de Castro et al. 2016; Karinkuzhi et al. 2018b; Shejeelammal et al. 2020) reported $[\text{Na}/\text{Fe}] \gtrsim +0.4$ dex for Ba giants, and de Castro et al. (2016) observed an anticorrelation between $[\text{Na}/\text{Fe}]$ and $\log g$ for the stars of their sample (see their Figure 20).

Na production is also associated with nucleosynthesis in AGB stars. Models predict that AGB stars are able to produce ^{23}Na from Ne isotopes, through the NeNa chain of proton capture, via $^{22}\text{Ne}(p,\gamma)^{23}\text{Na}$ reaction, where the ^{22}Ne was previously synthesized in the He-burning shell, from the $^{14}\text{N}(\alpha,\gamma)^{18}\text{F}(\beta^+)^{18}\text{O}(\alpha,\gamma)^{22}\text{Ne}$ reaction sequences (e.g., Mowlavi 1999; Karakas & Lattanzio 2014). The processed material is mixed and brought to the AGB atmosphere, via the third dredge-up (TDU), and then is subsequently transferred to the observed Ba star. However, no Na enhancement is observed in our stars.

5.3. Neutron-capture Elements

Elements beyond the iron peak ($Z > 30$) are primarily synthesized throughout neutron captures on seed nuclei, the s -process and the so-called r - (*rapid*) process, depending on the time involved between neutron captures and β decays. While the s -process takes place within TP-AGB stars, the exact astrophysical site(s) of the r -process is(are) a matter of debate, although supernovae events and neutron star mergers figure among the most promising scenarios (see the review of Cowan et al. 2021). As far as heavy elements are concerned, we have derived elemental abundances of Sr, Y, Zr, Ba, La, Ce, Nd, Sm, Eu, and Pb. As anticipated in the Introduction, the chemical patterns of heavy elements observed in Ba stars help us to trace back their former polluter TP-AGB stars.

Table 8 lists the s -process contribution to the Solar system material, where we can see a high contribution of the s -process in the nucleosynthesis of the elements Sr, Y, Zr, Ba, La, Ce,

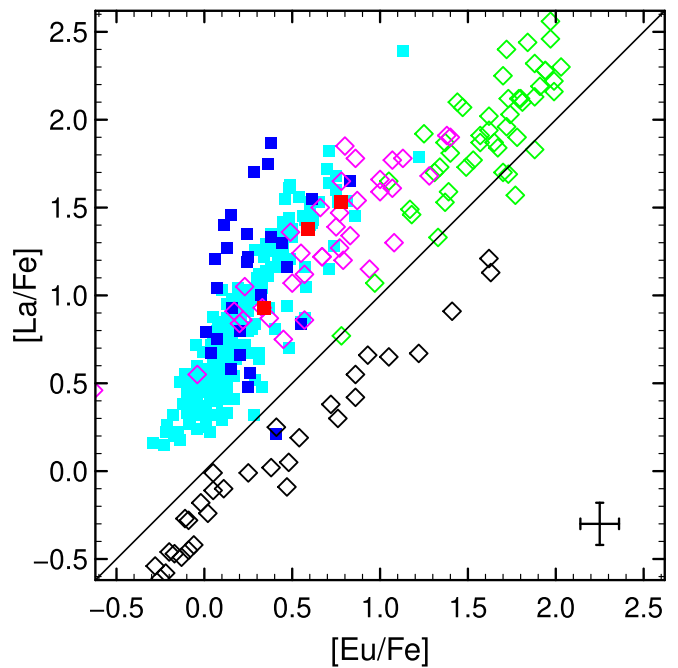


Figure 6. Program stars in the $[\text{La}/\text{Fe}]$ vs. $[\text{Eu}/\text{Fe}]$ plane, along with data for other Ba dwarfs and Ba giants. Symbols and the literature references are the same as in the caption of Figure 4. Diamonds are data for CEMP- r (black), CEMP- s (magenta), and CEMP- r/s (green), taken from Masseron et al. (2010) and Karinkuzhi et al. (2021).

and Nd. Indeed, they are found very abundant in our targets, with $[\text{X}/\text{Fe}]$ ratios $\gtrsim +1.00$ dex, evidencing the strong s -rich nature of these objects, while normal field stars show $[\text{X}/\text{Fe}]$ close to zero. Lead abundances are also enhanced in HD 15096, HD 141804, and HD 207585, with $[\text{Pb}/\text{Fe}] = +1.04$, $+1.46$, and $+1.35$ dex, respectively. For HD 37792, we were able to report only the upper limit $[\text{Pb}/\text{Fe}] < +0.50$ dex. Data on lead abundances, however, are very scarce in the literature. For the element samarium, which has a low s -process contribution (see Table 8), we also found excesses in our stars ($+0.80 < [\text{Sm}/\text{Fe}] < +1.35$). These high levels are not effects of the Galactic chemical evolution and are found in Ba giants and other Ba dwarfs (Allen & Barbuy 2006a). Europium, a representative element of the r -process, shows slightly enhanced abundances in our stars, with $[\text{Eu}/\text{Fe}]$ values of $+0.34$, $+0.78$, and $+0.59$ dex for HD 15096, HD 141804, and HD 207585, respectively. For HD 37792, europium abundance could not be derived, since the diagnostic spectral line was faintly detectable in its spectrum.

In Figure 6, we located our stars in the $[\text{La}/\text{Fe}]$ versus $[\text{Eu}/\text{Fe}]$ diagram, along with data available for other Ba dwarfs. We also added to this plot data for Ba giants and carbon-enhanced metal-poor (CEMP) stars (Beers & Christlieb 2005; Masseron et al. 2010). Since La and Eu are representative elements of the s - and r -processes, respectively, this diagram is able to split the data according to the neutron-capture levels of enrichment observed in the stars. As demonstrated in that figure, our stars share the same portion (the s -rich side) where other Ba dwarfs, Ba giants, and the CEMP- s lie.

5.3.1. The s -process Indexes

The $[\text{hs}/\text{ls}]$ ratio is an intrinsic s -process index, widely used to probe the neutron exposures of the s -process (e.g., Luck &

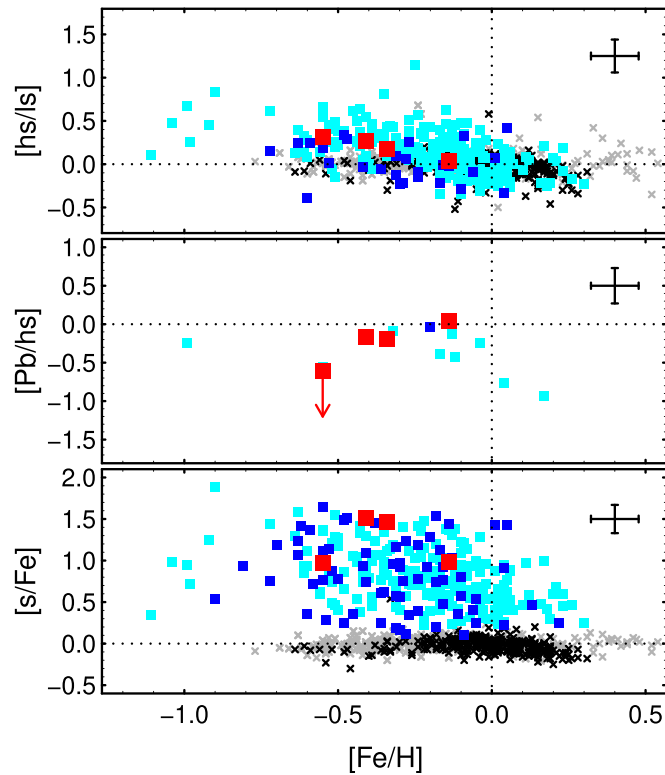


Figure 7. Indexes of the s -process. The upper, middle, and bottom panels show, respectively, the $[\text{hs}/\text{ls}]$, $[\text{Pb}/\text{hs}]$, and $[\text{s}/\text{Fe}]$ ratios as functions of the metallicity. Symbols and the literature references are the same as in the caption of Figure 4. Typical error bars for our data are also shown in the panels.

Bond 1991; Busso et al. 2001). This ratio is defined as the difference $[\text{hs}/\text{Fe}] - [\text{ls}/\text{Fe}]$, where $[\text{hs}/\text{Fe}]$ and $[\text{ls}/\text{Fe}]$ are the averaged abundances of the elements belonging to the second (Ba, La, Ce, Nd) and first (Sr, Y, Zr) s -process peaks. High neutron exposures push nucleosynthesis of the second peak elements, instead elements of the first peak, so that $[\text{hs}/\text{ls}] > 0$ is expected. HD 15096, HD 37792, HD 141804, and HD 207585, show $[\text{hs}/\text{ls}] = +0.04, +0.31, +0.27$, and $+0.17$ dex, respectively. As shown in the upper panel of Figure 7, these values are consistent with those reported in the literature for Ba stars. The $[\text{Pb}/\text{hs}]$ ratio is useful to probe the nucleosynthesis among the third (Pb) and second peaks. We found $[\text{Pb}/\text{hs}] = +0.04, -0.61, -0.17$, and -0.19 dex for HD 15096, HD 37792, HD 141804, and HD 207585, respectively. However, the literature lacks lead abundance data (see middle panel of Figure 7). Considering the $[\text{hs}/\text{ls}]$ and $[\text{Pb}/\text{hs}]$ ratios, we conclude that the neutron exposures favored the nucleosynthesis of the second peak elements.

We also computed the $[\text{s}/\text{Fe}]$ index, given by the s -process average abundances from elemental abundances for Sr, Y, Zr, Ba, La, Ce, Nd, and Pb, yielding $[\text{s}/\text{Fe}] = +0.99, +0.92, +1.10$, and $+1.45$ dex for HD 15096, HD 37792, HD 141804, and HD 207585, respectively. Normal field stars typically show $[\text{s}/\text{Fe}] \sim 0$, whereas Ba stars exhibit $[\text{s}/\text{Fe}]$ ratios increasing for lower-metallicity regimes (see the bottom panel of Figure 7), a feature of the s -process (e.g., Busso et al. 2001). In their study on Ba giant stars, de Castro et al. (2016) assumed $[\text{s}/\text{Fe}] > +0.25$ dex as a criterion to classify a star as Ba star, and our stars satisfy this condition.

5.3.2. Mean Neutron Exposures

To infer quantitatively the neutron exposure levels to which the s -processed material observed in our targets was subjected, we have used the classical analysis of the main s -process component (Käppeler et al. 1990; Käppeler et al. 2011) to estimate the mean neutron exposures (τ_0). This approach consists of the so-called σN_s curve, which shows the behavior of the product between the neutron-capture cross sections (σ) and the abundances of the main s -process component (N_s), traditionally expressed in the scale $\log \epsilon(\text{Si}) = 6.0$. The σN_s curve is written in terms of τ_0 and G , which are free parameters to fit the observations, where G is the fraction of ^{56}Fe used as the seed of the s -process. G has the effect of shifting the curve, while τ_0 changes the shape of the σN_s curve. An interesting feature of the classical approach is that it successfully reproduces the main component of the s -process of the solar system, with $\tau_0 \sim 0.30 \text{ mb}^{-1}$ (Arlandini et al. 1999), even without any assumption of the astrophysical site of the s -process.

From their abundance data in Ba stars, Allen & Barbuy (2006b) extracted abundances owing the main component of the s -process, and were able to estimate the neutron exposures for the stars of their sample, fitting σN_s curves to the observed data. For a detailed description of that procedure, we refer the reader to the respective paper. Here, we have applied a similar procedure to evaluate τ_0 in our targets. In order to test our algorithm, we downloaded from the KADoNiS⁹ database a list of neutron-capture cross sections (at 30 keV) and computed, via χ^2 minimization, the best σN_s curve that reproduces the main component of the s -process for the solar distribution reported by Arlandini et al. (1999). With our implementation, we found $\tau_0 = 0.36 \text{ mb}^{-1}$, close to the value of Arlandini et al.; in their methodology, Allen & Barbuy found $\tau_0 \sim 0.35 \text{ mb}^{-1}$. Extending that approach for HD 15096, HD 37792, HD 141804, and HD 207585, we found $\tau_0 = 0.55, 0.58, 0.75$, and 0.61 mb^{-1} , respectively. Figure 8 shows the best fits of the σN_s curves to the observed data. In a recent review, Lugaro et al. (2023) comment that the ^{13}C neutron source (see next section) provides neutron exposure values up to 1.0 mb^{-1} , which validates the results derived from our simple approach. Allen & Barbuy reported τ_0 values ranging from 0.187 to 1.05 mb^{-1} for the Ba stars of their sample.

6. Comparison with s -process Nucleosynthesis Models

Various groups have computed theoretical s -process yields from their AGB stellar models. In particular, the models provided by the INAF group (Cristallo et al. 2009, 2011, 2015)—through the online FRUITY¹⁰ database—and Monash group (Fishlock et al. 2014; Karakas & Lugaro 2016; Karakas et al. 2018) comprise predictions for a wide range of masses ($1.0 \leq M/M_\odot \leq 8.0$) and metallicities ($-1.2 \lesssim [\text{Fe}/\text{H}] \lesssim +0.3$), which covers the interval observed in Ba stars.

TP-AGB stars provide a conducive environment for the s -process nucleosynthesis within a tenuous He-rich region (He intershell) located between the H- and He-burning shells, which are activated alternately in this evolutionary stage (Busso et al. 1999; Straniero et al. 2006; Käppeler et al. 2011; Karakas &

⁹ Karlsruhe Astrophysical Database of Nucleosynthesis in Stars; available at <https://www.kadonis.org/>.

¹⁰ FRUITY-Network Repository of Updated Isotopic Tables and Yields, at <http://fruity.oa-teramo.inaf.it/>.

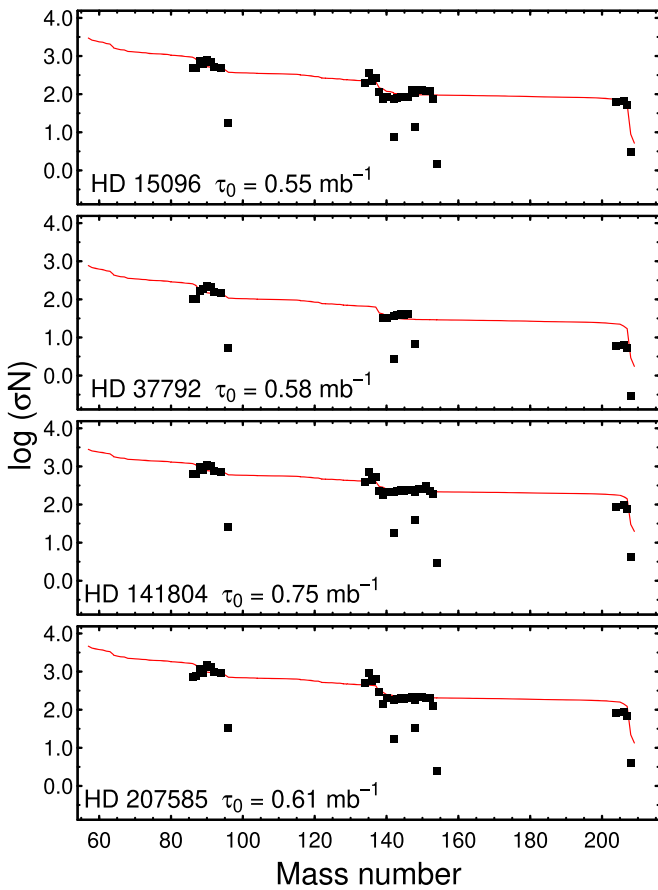


Figure 8. Fitting of theoretical σN_s curves (red lines) and observed σN_s values (black squares). The data are plotted in logarithmic scale; σ is expressed in millibarn and N_s in the scale $\log \epsilon(\text{Si}) = 6.0$. The estimated neutron exposures are shown in the bottom of panels.

Lattanzio 2014; Lugaro et al. 2023). For low-mass ($1\text{--}3 M_\odot$) AGB stars, the $^{13}\text{C}(\alpha, n)^{16}\text{O}$ reaction provides the main supply of neutrons to feed the s -process, during the interpulse periods (H-burning shell). This reaction is efficiently activated at $T \sim 10^8$ K, releasing within the He intershell a relatively low neutron density, on the order of $10^{7\text{--}8} \text{ cm}^{-3}$ (Straniero et al. 1995, 1997). The H-burning ashes accumulate in the inner layers and trigger periodically He flashes (thermal pulses; TP) that, in turn, expand the upper layers of the stars. As a consequence, the H burning in a shell is temporarily extinguished and a convective zone is driven in the He intershell. Temperatures in this region can reach values high enough to activate an alternative neutron source, the $^{22}\text{Ne}(\alpha, n)^{25}\text{Mg}$ reaction. However, for low-mass AGB stars, this reaction is only marginally activated. After a limited number of TP episodes, the base of the extensive convective envelope can deepen its base, carrying to the stellar surface (the TDU) the by-products of the internal nucleosynthesis, rich in carbon and s -elements. The $^{22}\text{Ne}(\alpha, n)^{25}\text{Mg}$ reaction becomes the main neutron provider for AGB stars of intermediate masses ($4\text{--}8 M_\odot$), during the TP events, at temperatures higher than 3×10^8 K, releasing a neutron burst of $10^{10\text{--}12} \text{ cm}^{-3}$.

The FRUITY and Monash models are based on different stellar evolution codes, which assume different physical and nuclear inputs. Additionally, these models adopt different approaches to perform their detailed nucleosynthesis computations, mainly regarding the formation of the ^{13}C pocket, since

the ^{13}C left in the He intershell is not able to provide the required neutron densities to reproduce the observations (Busso et al. 1995; Abia et al. 2001; Busso et al. 2001). To address this challenge, modelers assume the occurrence of proton ingestion in the He intershell at the time of the TDU, which leads to the formation of a ^{13}C pocket in the next interpulse period and provides the neutron reservoir to the s -process (Straniero et al. 1995, 1997). However, this standard approach introduces the major uncertainty source in the predictions (see, e.g., Karakas & Lattanzio 2014). The FRUITY models self-consistently produce the ^{13}C pocket from a time-dependent convective overshoot implementation (Cristallo et al. 2009). In the Monash models, a parametric approach leads to the ^{13}C pocket formation, by artificially inserting a mass of protons (controlled by the M_{mix} parameter) in the top layers of the He intershell during the TDU (Lugaro et al. 2012). A detailed comparison between the FRUITY and Monash models is presented by Karakas & Lugaro (2016).

In this section, we perform a target-to-target comparison between the observed abundance patterns in our stars and those predicted by the (nonrotating) FRUITY and Monash models. For this, we have collected the $[X/\text{Fe}]$ ratios predicted by these models, computed after the last TP, at the AGB surface. However, the s -processed material transferred was further diluted in the atmosphere of the observed Ba star. To take these effects into account, we must introduce a dilution factor (dil) in the predictions. This parameter is defined as the ratio $\log(M_{\text{Ba}}^{\text{env}}/M_{\text{AGB}}^{\text{transf}})$, where $M_{\text{Ba}}^{\text{env}}$ is the mass of the envelope of the Ba star after mass transfer and $M_{\text{AGB}}^{\text{transf}}$ is the mass transferred from the former AGB star. In this way, the diluted $[X/\text{Fe}]_{\text{Ba}}$ ratio expected to be observed in Ba stars is given by the parametric equation:

$$[X/\text{Fe}]_{\text{Ba}} = \log [f \times 10^{[X/\text{Fe}]_{\text{ini}}} + 10^{[X/\text{Fe}]_{\text{AGB}} - \text{dil}}], \quad (5)$$

where $f = 1 - 10^{\text{dil}}$, $[X/\text{Fe}]_{\text{ini}}$ is the initial (solar) composition adopted in the models and $[X/\text{Fe}]_{\text{AGB}}$ is the final abundance predicted by the models. The dilution factor has the effect of lowering the predicted abundances but without changing the shape of the distribution. Previous studies adopted that methodology in order to derive dilution factors and infer the mass of the AGB progenitor star (see, e.g., Husti et al. 2009; Shejeelammal et al. 2020; Cseh et al. 2022). We have applied different dilution factors to each model of our grid and compared the diluted predictions to the observed abundance patterns, evaluating the quality of the fits from the χ^2 values. From a χ^2 minimization, we find the models that best fit the observed data, and consequently the dilution factors.

In Figure 9, we show the neutron-capture patterns observed in HD 15096, HD 37792, HD 141804, and HD 207585, and the Monash and FRUITY models that best fit the observations. We can see that s -process nucleosynthesis models for low-mass ($\leq 3.0 M_\odot$) AGB stars are able to reproduce successfully our observations. In their analysis, using the FRUITY models, Shejeelammal et al. (2020) fitted the abundance pattern of HD 207585 with a $2.5 M_\odot$ ($Z = 0.008$) model. Our results are consistent with many other studies that have evidenced the low-mass nature of the former polluter TP-AGB stars that contaminated the envelope of Ba stars (e.g., Allen & Barbay 2006a; Karinkuzhi et al. 2018b; Cseh et al. 2018, 2022; Shejeelammal et al. 2020; den Hartogh et al. 2023). In connection, this favors ^{13}C as the main neutron

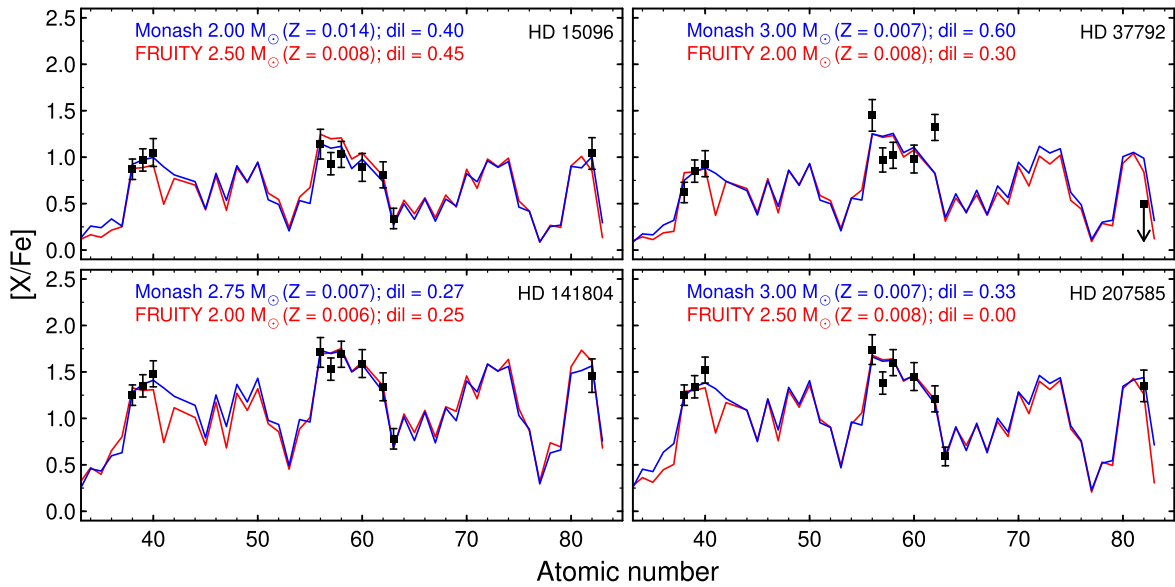


Figure 9. Comparison between the observed abundance profiles (black squares with error bars) and the predicted profiles (curves) from the Monash (blue) and FRUITY (red) nucleosynthesis models that best fit the observational data set, after dilution is applied. The derived dilution factors are also shown.

Table 9
Kinematic Data for the Ba Dwarfs Analyzed in This Work

Star	RV (km s^{-1})	U_{LSR} (km s^{-1})	V_{LSR} (km s^{-1})	W_{LSR} (km s^{-1})	P_{thin}	P_{thick}	P_{halo}
HD 15096	-5.62 ± 0.19	-30.5 ± 0.5	-7.0 ± 0.2	$+42.5 \pm 0.4$	0.95	0.05	0.00
HD 37792	$+10.13 \pm 0.44$	$+56.0 \pm 1.5$	-10.7 ± 0.6	-56.5 ± 1.7	0.76	0.23	0.00
HD 141806	-55.30 ± 0.41	-47.4 ± 0.4	$+23.4 \pm 0.4$	-10.8 ± 0.3	0.98	0.02	0.00
HD 207585	-55.89 ± 0.31	-21.6 ± 0.2	-39.7 ± 1.4	$+35.8 \pm 0.6$	0.88	0.12	0.00

Note. The radial velocities are given in the second column. The spacial velocities with their respective uncertainties are given from the third to fifth columns. The sixth, seventh, and eighth columns give the probability of a star being a member of the thin disk (P_{thin}), thick disk (P_{thick}), and halo (P_{halo}), respectively.

source powering the s -process in low-mass AGB stars. Furthermore, if TP-AGB stars of higher masses were responsible for the patterns observed in the program stars, it would be expected to find magnesium excesses in their atmospheres, in consequence of the operation of the ^{22}Ne neutron source. This is not observed in our stars, which exhibit normal $[\text{Mg}/\text{Fe}]$ ratios (see Tables 3 and 4). Concerning the dilution factors, low values were found ($\text{dil} \leq 0.45$), which is reasonable, since Ba dwarfs do not present extended atmospheres. Husty et al. (2009) reported $\text{dil} \lesssim 1.0$ for the Ba dwarfs of Allen & Barbuy (2006a). From the mass estimation of the polluted TP-AGB stars, we have applied the empirical initial-final mass relation of El-Badry et al. (2018) to constrain the masses of WD companions of our stars. We found $\langle M_{\text{WD}} \rangle \sim 0.66 M_{\odot}$, in agreement with values derived by Escorza & De Rosa (2023), who combined astrometric data in their analysis.

7. Kinematics

The kinematics properties of the Ba dwarfs analyzed in this work were obtained following the methodology outlined in de Castro et al. (2016). Distances and proper motions were obtained based on kinematic Gaia EDR3 data (Gaia Collaboration 2021) while radial velocities were obtained based on Doppler shift of the spectral absorption lines (Section 3.1). Then we determined the spatial velocities relative to the local

standard of rest, U_{LSR} , V_{LSR} , W_{LSR} , where U_{LSR} is positive toward the Galactic center, V_{LSR} is positive in the direction of Galactic rotation ($l=90^{\circ}$, $b=0^{\circ}$), and W_{LSR} is positive toward the north Galactic pole ($b=90^{\circ}$). We assumed the solar motion of $(11.1, 12.2, 7.3) \text{ km s}^{-1}$, as derived by Schönrich et al. (2010) and the algorithm of Johnson & Soderblom (1987). Finally, the probability of a Ba dwarf star belonging to the thin disk, thick disk, or halo population was calculated, following the procedure described in Ramírez et al. (2013). Membership to a given population was established when the star had a probability $P_{\text{population}}$ greater than or equal to 70%. Table 9 shows the results obtained for the spatial velocities and the corresponding probabilities.

Figure 10 displays the Toomre diagram of $(U_{\text{LSR}}^2 + W_{\text{LSR}}^2)^{1/2}$ versus V_{LSR} , where the stars are kinematically classified according to their spatial velocities and probabilities. In addition to the program stars, the position of some Ba dwarf stars analyzed by Pereira & Drake (2011); Escorza et al. (2019), and Pereira (2005) are also shown. Data for Ba giants are included in Figure 10. HD 15096, HD 37792, HD 141804, and HD 207585 exhibit kinematical properties consistent with thin disk stars, as indicated by their membership probabilities. Most of the previously analyzed Ba dwarfs also belong to the thin disk, with one exception for the star HD 6434, which can be considered as a thin-thick disk star with P_{thin} and P_{thick} probabilities of 33% and 66%, respectively.

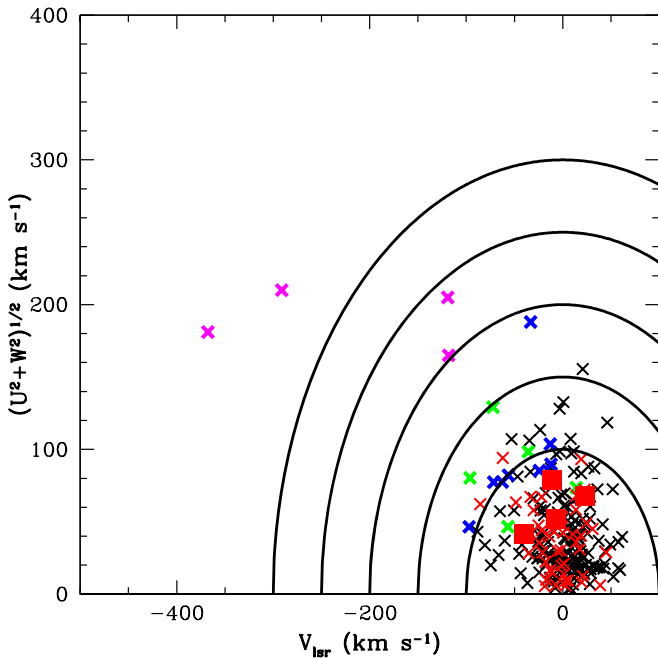


Figure 10. Ba dwarfs analyzed in this work (red squares) in the Toomre diagram of $(U_{\text{LSR}}^2 + W_{\text{LSR}}^2)^{1/2}$ vs. V_{LSR} . Ba dwarfs previously analyzed by Pereira & Drake (2011), Escorza et al. (2019), and Pereira (2005) are shown in red crosses. The classical Ba giant stars of the thin disk (black crosses), transition thin/thick disk (green crosses), thick disk (blue crosses), and halo (magenta crosses), taken from de Castro et al. (2016), are also plotted in this diagram.

8. Conclusions

We conducted a classical LTE analysis based on high-resolution spectroscopic data for a sample of four chemically peculiar stars. HD 15096, HD 37792, and HD 141804 were considered potential Ba dwarf candidates, whereas HD 207585 is a known Ba dwarf star. We have determined their atmospheric parameters, from clean and sufficiently unblended Fe I and Fe II absorption lines, and compared them with values previously reported in the literature. We found effective temperatures between 5300 and 6500 K, surface gravities within the interval $3.90 \leq \log g \leq 4.50$, and $-0.55 \leq [\text{Fe}/\text{H}] \leq +0.14$.

Subsequently, chemical abundances were extracted for a set of 21 elements, including the CNO group and neutron-capture elements. We found moderate carbon excesses in these stars, with $[\text{C}/\text{Fe}]$ ratios ranging from +0.29 to +0.66, and that carbon is mainly responsible for the CNO excesses observed in their atmospheres. HD 15096 and HD 37792 show $\text{C}/\text{O} < 1$, typical for Ba stars, while HD 141804 and HD 207585 show $\text{C}/\text{O} > 1$, typical for CH stars. For the elements from sodium to nickel, these systems follow the Galactic trend. On the other hand, as far as the s -process elements are concerned, the program stars show high levels of enrichment, with $[\text{s}/\text{Fe}] \gtrsim +1.00$ dex. All these stars are identified as spectroscopic binaries in the SIMBAD database, and orbital elements are provided in the literature for HD 15096, HD 141804, and HD 207585. Hence, their chemical peculiarities are attributable to mass-transfer events. We applied

the classical approach of the s -process (the σN_s curve) to estimate the mean neutron exposures of the s -processed material observed in their envelopes, yielding τ_0 on the order of $0.6\text{--}0.7 \text{ mb}^{-1}$.

We individually compared the observed abundance patterns in our stars with Monash and FRUITY nucleosynthesis models of the s -process. Consequently, we were able to estimate dilution factors and masses of the former polluting TP-AGB stars. Low-mass ($M \lesssim 3.0 M_{\odot}$) models successfully reproduced our observations. Notably, no Na enrichment was detected in the program stars, providing additional evidence for the operation of ^{13}C as the main neutron source of the TP-AGB stars. We applied the empirical initial–final mass relation of El-Badry et al. (2018) to estimate the masses of the WD companions of our stars, yielding $\langle M_{\text{WD}} \rangle \sim 0.66 M_{\odot}$, which is consistent for Ba and related stars. From the kinematic point of view, we estimated the probabilities of these stars belonging to thin disk, thick disk, and halo. We found that these objects are members of a thin disk, with probabilities greater than 70%.

In conclusion, we have identified HD 15096 and HD 37792 as two new Ba dwarfs and confirmed the Ba dwarf nature of HD 141804. As we pointed out, the current sample of Ba dwarfs confirmed from high-resolution spectroscopic data is much smaller than the sample of the classical giants. Therefore, we stressed on the need of identifying new Ba dwarf star candidates and exploring their chemical patterns.

Acknowledgments

This work has been developed under a fellowship of the PCI Program of the Ministry of Science, Technology and Innovation—MCTI; financed by the Brazilian National Council of Research—CNPq, through grant 301140/2024-3. N.H. acknowledges the fellowships (300181/2023-0, 300434/2024-3, and 301126/2024-0) of the PCI Program—MCTI and CNPq. N.A.D. acknowledges Fundação de Amparo à Pesquisa do Estado do Rio de Janeiro—FAPERJ, Rio de Janeiro, Brazil, for grant E-26/203.847/2022. A.S. acknowledges CNPq for a PhD fellowship 141219/2023-8. This work has made use of the VALD database, operated at Uppsala University, the Institute of Astronomy RAS in Moscow, and the University of Vienna. This research has made use of NASA’s Astrophysics Data System Bibliographic Services.

Software: IRAF (Tody 1986); MOOG (Sneden 1973; Sneden et al. 2012); R and RStudio (R Core Team 2021).

Appendix

Table 10 lists the wavelengths, excitation potentials, and $\log gf$ values adopted in this work for the iron lines, as well as their respective EW measurements. For the atomic lines of the other elements analyzed, the adopted lab data and EW measurements are provided in Table 11. Tables 10 and 11 are available in a machine-readable format. A portion is shown here for guidance regarding its form and content.

Table 10
Equivalent Width Measurements of Fe I and Fe II Lines [Example]

Element	Wavelength	χ (eV)	$\log gf$	Equivalent Widths (mÅ)			
				HD 15096	HD 37792	HD 141804	HD 207585
Fe I	5133.69	4.18	+0.20	108	...
	5150.84	0.99	-3.00	135	58	75	...
	5151.91	1.01	-3.32	...	41
	5159.06	4.28	-0.65	77	28	39	53
	5162.27	4.18	+0.07	...	80
	5194.94	1.56	-2.09	...	80	91	109
	5198.71	2.22	-2.14	111	49	63	76
	5232.94	2.94	-0.08	...	117
	5242.49	3.63	-0.97	93	48	54	71
	5250.21	0.12	-4.92	80	50

Fe II	4993.35	2.81	-3.67	31	25	28	41
	5132.66	2.81	-4.00	17
	5197.56	3.23	-2.25	64
	5234.62	3.22	-2.24	66	84	74	83
	5284.10	2.89	-3.01	51	...	49	63
	5325.56	3.22	-3.17	29	34	32	38
	5414.05	3.22	-3.62	16	19	20	...
	5425.25	3.20	-3.21	31	33	34	49
	5534.83	3.25	-2.77	43	55	45	...
	5991.37	3.15	-3.56	21	21	22	30
	6084.10	3.20	-3.80	12	15	14	21
	6149.25	3.89	-2.72	22	29	26	35
	6247.55	3.89	-2.34	34	52	47	53
	6416.92	3.89	-2.68	27	27	32	33
	6432.68	2.89	-3.58	...	32	...	38

Note.

(This table is available in its entirety in machine-readable form.)



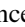

Table 11
Atomic Line Lists for Other Chemical Species [Example]

Element	Wavelength	χ (eV)	$\log gf$	References	Equivalent Widths (mÅ)			
					HD 15096	HD 37792	HD 141804	HD 207585
C I	4770.03	7.48	-2.33	(T02)	...	17	22	21
	4775.90	7.49	-2.19	(T02)	11	22	30	...
	4932.05	7.69	-1.66	(T02)	...	33	53	...
	5052.10	7.68	-1.30	(T02)	26	49	67	70
	5380.34	7.68	-1.84	(T02)	...	33	43	45
	6587.60	8.54	-1.22	(L82)	...	27	...	38
	7111.48	8.64	-1.32	(L82)	...	17	...	24
	7113.18	8.64	-0.95	(L82)	...	30	43	37
	7115.19	8.64	-0.90	(L82)	...	30	40	47
	7116.99	8.64	-1.08	(L82)	...	25	32	37
	9061.48	7.48	-0.34	(TS97)	177	...
	9078.32	7.48	-0.58	(TS97)	...	160	...	156
	9111.85	7.49	-0.29	(TS97)	105
	Sm II
4318.94		0.28	-0.25	(L06)	47
4360.71		0.25	-0.87	(L06)	...	16
4362.02		0.48	-0.47	(L06)	...	19
4467.34		0.66	+0.15	(L06)	34	...	42	50
4499.48		0.25	-0.87	(L06)	15	...	19	32
4523.91		0.43	-0.39	(L06)	36
4566.20		0.33	-0.59	(L06)	22	...	22	39
4676.90		0.04	-0.87	(L06)	23	...
4704.40		0.00	-0.86	(L06)	24	...	29	39
4791.60		0.10	-1.44	(L06)	10	14

References. (C2003) Chen et al. (2003); (Ca2007) Carretta et al. (2007); (D2002) Depagne et al. (2002); (DH) Den Hartog et al. (2003); (DS91) Drake & Smith (1991); (E93) Edvardsson et al. (1993); (J2006) Johnson et al. (2006); (L01) Lawler et al. (2001a); (L06) Lawler et al. (2006); (L09) Lawler et al. (2009); (L13) Lawler et al. (2013); (L82) Lambert et al. (1982); (Lj06) Ljung et al. (2006); (MR94) McWilliam & Rich (1994); (N96) Norris et al. (1996); (PS) Preston & Sneden (2001); (R03) Reddy et al. (2003); (R04) Reyniers et al. (2004); (R99) Reddy et al. (1999); (S07) Sobek et al. (2007); (S86) Smith et al. (1986); (SN96) Sneden et al. (1996); (T02) Takeda et al. (2002); (TH05) Takeda & Honda (2005); (TS97) Takeda & Sadakane (1997); (VWR) Van Winckel & Reyniers (2000); (W14) Wood et al. (2014); (WSM) Wiese et al. (1969).

(This table is available in its entirety in machine-readable form.)

ORCID iDs

M. P. Roriz  <https://orcid.org/0000-0001-9164-2882>
 N. Holanda  <https://orcid.org/0000-0002-8504-6248>
 L. V. da Conceição  <https://orcid.org/0000-0002-5042-443X>
 N. A. Drake  <https://orcid.org/0000-0003-4842-8834>

References

- Abia, C., Busso, M., Gallino, R., et al. 2001, *ApJ*, 559, 1117
 Allen, D. M., & Barbuy, B. 2006a, *A&A*, 454, 895
 Allen, D. M., & Barbuy, B. 2006b, *A&A*, 454, 917
 Allende Prieto, C., Lambert, D. L., & Asplund, M. 2001, *ApJL*, 556, L63
 Alonso, A., Arribas, S., & Martínez-Roger, C. 1995, *A&A*, 297, 197
 Amarsi, A. M., Asplund, M., Collet, R., & Leenaarts, J. 2015, *MNRAS*, 454, L11
 Antipova, L. I., Boyarchuk, A. A., Pakhomov, Y. V., & Panchuk, V. E. 2004, *ARep*, 48, 597
 Arlandini, C., Käppeler, F., Wisshak, K., et al. 1999, *ApJ*, 525, 886
 Barbuy, B., Jorissen, A., Rossi, S. C. F., & Arnould, M. 1992, *A&A*, 262, 216
 Beers, T. C., & Christlieb, N. 2005, *ARA&A*, 43, 531
 Bessell, M. S., Castelli, F., & Plez, B. 1998, *A&A*, 333, 231
 Bidelman, W. P., & Keenan, P. C. 1951, *ApJ*, 114, 473
 Bisterzo, S., Travaglio, C., Gallino, R., Wiescher, M., & Käppeler, F. 2014, *ApJ*, 787, 10
 Bond, H. E. 1974, *ApJ*, 194, 95
 Boothroyd, A. I., Sackmann, I. J., & Wasserburg, G. J. 1995, *ApJL*, 442, L21
 Bressan, A., Marigo, P., Girardi, L., et al. 2012, *MNRAS*, 427, 127
 Burbidge, E. M., Burbidge, G. R., Fowler, W. A., & Hoyle, F. 1957, *RvMP*, 29, 547
 Busso, M., Gallino, R., Lambert, D. L., Travaglio, C., & Smith, V. V. 2001, *ApJ*, 557, 802
 Busso, M., Gallino, R., & Wasserburg, G. J. 1999, *ARA&A*, 37, 239
 Busso, M., Lambert, D. L., Beglio, L., et al. 1995, *ApJ*, 446, 775
 Carretta, E., Bragaglia, A., & Gratton, R. G. 2007, *A&A*, 473, 129
 Chen, B., Vergely, J. L., Valette, B., & Carraro, G. 1998, *A&A*, 336, 137
 Chen, Y. Q., Zhao, G., Nissen, P. E., Bai, G. S., & Qiu, H. M. 2003, *ApJ*, 591, 925
 Cowan, J. J., Sneden, C., Lawler, J. E., et al. 2021, *RvMP*, 93, 015002
 Cristallo, S., Piersanti, L., Straniero, O., et al. 2011, *ApJS*, 197, 17
 Cristallo, S., Straniero, O., Gallino, R., et al. 2009, *ApJ*, 696, 797
 Cristallo, S., Straniero, O., Piersanti, L., & Gobrecht, D. 2015, *ApJS*, 219, 40
 Cseh, B., Lugaro, M., D'Orazi, V., et al. 2018, *A&A*, 620, A146
 Cseh, B., Világos, B., Roriz, M. P., et al. 2022, *A&A*, 660, A128
 da Silva, L., Girardi, L., Pasquini, L., et al. 2006, *A&A*, 458, 609
 de Castro, D. B., Pereira, C. B., Roig, F., et al. 2016, *MNRAS*, 459, 4299
 de Strobel, G. C., & Spite, M. (ed.) 1988, in IAU Symp. 132, The Impact of very High S/N Spectroscopy on Stellar Physics (Dordrecht: Kluwer)
 Den Hartog, E. A., Lawler, J. E., Sneden, C., & Cowan, J. J. 2003, *ApJS*, 148, 543
 den Hartogh, J. W., Yagüe López, A., Cseh, B., et al. 2023, *A&A*, 672, A143
 Depagne, E., Hill, V., Spite, M., et al. 2002, *A&A*, 390, 187
 Drake, J. J., & Smith, G. 1991, *MNRAS*, 250, 89
 Drake, N. A., & Pereira, C. B. 2007, in Convection in Astrophysics, ed. F. Kupka, I. Roxburgh, & K. L. Chan, Vol. 239 (Cambridge: Cambridge Univ. Press), 304
 Drake, N. A., & Pereira, C. B. 2008, *AJ*, 135, 1070
 Edvardsson, B., Andersen, J., Gustafsson, B., et al. 1993, *A&A*, 275, 101
 El-Badry, K., Rix, H.-W., & Weisz, D. R. 2018, *ApJL*, 860, L17
 Escorza, A., Boffin, H. M. J., Jorissen, A., et al. 2017, *A&A*, 608, A100
 Escorza, A., & De Rosa, R. J. 2023, *A&A*, 671, A97
 Escorza, A., Karinkuzhi, D., Jorissen, A., et al. 2019, *A&A*, 626, A128

- Escorza, A., Siess, L., Van Winckel, H., & Jorissen, A. 2020, *A&A*, **639**, A24
- Fishlock, C. K., Karakas, A. I., Lugaro, M., & Yong, D. 2014, *ApJ*, **797**, 44
- Frantsman, Y. L. 1992, *SvA*, **36**, 155
- Fulbright, J. P. 2000, *AJ*, **120**, 1841
- Gaia Collaboration 2020, *yCat*, I/350
- Gaia Collaboration 2021, *A&A*, **649**, A1
- Gallino, R., Arlandini, C., Busso, M., et al. 1998, *ApJ*, **497**, 388
- Goswami, A., Aoki, W., Beers, T. C., et al. 2006, *MNRAS*, **372**, 343
- Goswami, A., Aoki, W., & Karinkuzhi, D. 2016, *MNRAS*, **455**, 402
- Gratton, R. G., Carretta, E., Claudi, R., Lucatello, S., & Barbieri, M. 2003, *A&A*, **404**, 187
- Grevesse, N., & Sauval, A. J. 1998, *SSRv*, **85**, 161
- Guo, F., Cheng, Z., Kong, X., et al. 2023, *AJ*, **165**, 40
- Han, Z., Eggleton, P. P., Podsiadlowski, P., & Tout, C. A. 1995, *MNRAS*, **277**, 1443
- Holanda, N., Drake, N. A., & Pereira, C. B. 2020, *MNRAS*, **498**, 77
- Holanda, N., Drake, N. A., & Pereira, C. B. 2023, *MNRAS*, **518**, 4038
- Husti, L., Gallino, R., Bisterzo, S., Straniero, O., & Cristallo, S. 2009, *PASA*, **26**, 176
- Johnson, D. R. H., & Soderblom, D. R. 1987, *AJ*, **93**, 864
- Johnson, J. A., Ivans, I. I., & Stetson, P. B. 2006, *ApJ*, **640**, 801
- Jorissen, A., Boffin, H. M. J., Karinkuzhi, D., et al. 2019, *A&A*, **626**, A127
- Jorissen, A., Van Eck, S., Mayor, M., & Udry, S. 1998, *A&A*, **332**, 877
- Jorissen, A., Van Eck, S., Van Winckel, H., et al. 2016, *A&A*, **586**, A158
- Kaeppler, F., Gallino, R., Busso, M., Picchio, G., & Raiteri, C. M. 1990, *ApJ*, **354**, 630
- Käppeler, F., Gallino, R., Bisterzo, S., & Aoki, W. 2011, *RvMP*, **83**, 157
- Karakas, A. I., & Lattanzio, J. C. 2014, *PASA*, **31**, e030
- Karakas, A. I., & Lugaro, M. 2016, *ApJ*, **825**, 26
- Karakas, A. I., Lugaro, M., Carlos, M., et al. 2018, *MNRAS*, **477**, 421
- Karinkuzhi, D., & Goswami, A. 2014, *MNRAS*, **440**, 1095
- Karinkuzhi, D., & Goswami, A. 2015, *MNRAS*, **446**, 2348
- Karinkuzhi, D., Goswami, A., Sridhar, N., Masseron, T., & Purandardas, M. 2018a, *MNRAS*, **476**, 3086
- Karinkuzhi, D., Van Eck, S., Jorissen, A., et al. 2018b, *A&A*, **618**, A32
- Karinkuzhi, D., Van Eck, S., Jorissen, A., et al. 2021, *A&A*, **654**, A140
- Kaufner, A., Stahl, O., Tubbesing, S., et al. 1999, *Msngr*, **95**, 8
- Keenan, P. C. 1942, *ApJ*, **96**, 101
- Kong, X. M., Bharat Kumar, Y., Zhao, G., et al. 2018, *MNRAS*, **474**, 2129
- Kurucz, R. 1993, *ATLAS9 Stellar Atmosphere Programs and 2 km/s grid*. Kurucz CD-ROM No. 13. Cambridge, 13
- Lambert, D. L., Heath, J. E., Lemke, M., & Drake, J. 1996, *ApJS*, **103**, 183
- Lambert, D. L., Roby, S. W., & Bell, R. A. 1982, *ApJ*, **254**, 663
- Latham, D. W., Stefanik, R. P., Torres, G., et al. 2002, *AJ*, **124**, 1144
- Lawler, J. E., Bonvallet, G., & Sneden, C. 2001a, *ApJ*, **556**, 452
- Lawler, J. E., Den Hartog, E. A., Sneden, C., & Cowan, J. J. 2006, *ApJS*, **162**, 227
- Lawler, J. E., Guzman, A., Wood, M. P., Sneden, C., & Cowan, J. J. 2013, *ApJS*, **205**, 11
- Lawler, J. E., Sneden, C., Cowan, J. J., Ivans, I. I., & Den Hartog, E. A. 2009, *ApJS*, **182**, 51
- Lawler, J. E., Wickliffe, M. E., den Hartog, E. A., & Sneden, C. 2001b, *ApJ*, **563**, 1075
- Liu, S., Wang, L., Shi, J.-R., et al. 2021, *RAA*, **21**, 278
- Ljung, G., Nilsson, H., Asplund, M., & Johansson, S. 2006, *A&A*, **456**, 1181
- Luck, R. E., & Bond, H. E. 1982, *ApJ*, **259**, 792
- Luck, R. E., & Bond, H. E. 1991, *ApJS*, **77**, 515
- Luck, R. E., & Heiter, U. 2006, *AJ*, **131**, 3069
- Luck, R. E., & Heiter, U. 2007, *AJ*, **133**, 2464
- Lugaro, M., Karakas, A. I., Stancliffe, R. J., & Rijs, C. 2012, *ApJ*, **747**, 2
- Lugaro, M., Pignatari, M., Reifarth, R., & Wiescher, M. 2023, *ARNPS*, **73**, 315
- Masseron, T., Johnson, J. A., Plez, B., et al. 2010, *A&A*, **509**, A93
- McClure, R. D. 1984, *ApJL*, **280**, L31
- McClure, R. D., Fletcher, J. M., & Nemeč, J. M. 1980, *ApJL*, **238**, L35
- McClure, R. D., & Woodworth, A. W. 1990, *ApJ*, **352**, 709
- McWilliam, A. 1998, *AJ*, **115**, 1640
- McWilliam, A., & Rich, R. M. 1994, *ApJS*, **91**, 749
- Mowlavi, N. 1999, *A&A*, **350**, 73
- Norfolk, B. J., Casey, A. R., Karakas, A. I., et al. 2019, *MNRAS*, **490**, 2219
- Norris, J. E., Ryan, S. G., & Beers, T. C. 1996, *ApJS*, **107**, 391
- North, P., Berthet, S., & Lanz, T. 1994, *A&A*, **281**, 775
- North, P. L., Jorissen, A., Escorza, A., Miszalski, B., & Mikolajewska, J. 2020, *Obs*, **140**, 11
- Pereira, C. B. 2005, *AJ*, **129**, 2469
- Pereira, C. B., & Drake, N. A. 2009, *A&A*, **496**, 791
- Pereira, C. B., & Drake, N. A. 2011, *AJ*, **141**, 79
- Pereira, C. B., Drake, N. A., & Roig, F. 2019, *MNRAS*, **488**, 482
- Pereira, C. B., Jilinski, E., Drake, N. A., et al. 2012, *A&A*, **543**, A58
- Pereira, C. B., & Junqueira, S. 2003, *A&A*, **402**, 1061
- Pereira, C. B., Sales Silva, J. V., Chavero, C., Roig, F., & Jilinski, E. 2011, *A&A*, **533**, A51
- Porto de Mello, G. F., & da Silva, L. 1997, *ApJL*, **476**, L89
- Pourbaix, D., Tokovinin, A. A., Batten, A. H., et al. 2004, *A&A*, **424**, 727
- Preston, G. W., & Sneden, C. 2001, *AJ*, **122**, 1545
- Purandardas, M., Goswami, A., Goswami, P. P., Shejeelammal, J., & Masseron, T. 2019, *MNRAS*, **486**, 3266
- Ramírez, I., Allende Prieto, C., & Lambert, D. L. 2013, *ApJ*, **764**, 78
- R Core Team 2021, *R: A Language and Environment for Statistical Computing* (Vienna: R Foundation for Statistical Computing), <https://www.R-project.org/>
- Reddy, B. E., Bakker, E. J., & Hrivnak, B. J. 1999, *ApJ*, **524**, 831
- Reddy, B. E., Lambert, D. L., & Allende Prieto, C. 2006, *MNRAS*, **367**, 1329
- Reddy, B. E., Tomkin, J., Lambert, D. L., & Allende Prieto, C. 2003, *MNRAS*, **340**, 304
- Reyniers, M., Van Winckel, H., Gallino, R., & Straniero, O. 2004, *A&A*, **417**, 269
- Roriz, M., Pereira, C. B., Drake, N. A., Roig, F., & Silva, J. V. S. 2017, *MNRAS*, **472**, 350
- Roriz, M. P., Lugaro, M., Pereira, C. B., et al. 2021a, *MNRAS*, **501**, 5834
- Roriz, M. P., Lugaro, M., Pereira, C. B., et al. 2021b, *MNRAS*, **507**, 1956
- Roriz, M. P., Pereira, C. B., Junqueira, S., et al. 2023, *MNRAS*, **518**, 5414
- Ryabchikova, T., Piskunov, N., Kurucz, R. L., et al. 2015, *PhyS*, **90**, 054005
- Schönrich, R., Binney, J., & Dehnen, W. 2010, *MNRAS*, **403**, 1829
- Shejeelammal, J., Goswami, A., Goswami, P. P., Rathour, R. S., & Masseron, T. 2020, *MNRAS*, **492**, 3708
- Smith, G., Edvardsson, B., & Frisk, U. 1986, *A&A*, **165**, 126
- Smith, V. V., Coleman, H., & Lambert, D. L. 1993, *ApJ*, **417**, 287
- Smith, V. V., & Lambert, D. L. 1986, *ApJ*, **303**, 226
- Sneden, C., Bean, J., Ivans, I., Lucatello, S., & Sobeck, J., 2012 MOOG: LTE Line Analysis and Spectrum Synthesis, Astrophysics Source Code Library, [ascl:1202.009](https://ui.adsabs.org/abs/2012ASCl..12000009S)
- Sneden, C., & Bond, H. E. 1976, *ApJ*, **204**, 810
- Sneden, C., McWilliam, A., Preston, G. W., et al. 1996, *ApJ*, **467**, 819
- Sneden, C. A. 1973, PhD thesis, The University of Texas at Austin
- Sobeck, J. S., Lawler, J. E., & Sneden, C. 2007, *ApJ*, **667**, 1267
- Soubiran, C., & Girard, P. 2005, *A&A*, **438**, 139
- Straniero, O., Chieffi, A., Limongi, M., et al. 1997, *ApJ*, **478**, 332
- Straniero, O., Gallino, R., Busso, M., et al. 1995, *ApJL*, **440**, L85
- Straniero, O., Gallino, R., & Cristallo, S. 2006, *NuPhA*, **777**, 311
- Takeda, Y., & Honda, S. 2005, *PASJ*, **57**, 65
- Takeda, Y., Parthasarathy, M., Aoki, W., et al. 2002, *PASJ*, **54**, 765
- Takeda, Y., & Sadakane, K. 1997, *PASJ*, **49**, 571
- Tody, D. 1986, *Proc. SPIE*, **627**, 733
- Tomkin, J., Lambert, D. L., Edvardsson, B., Gustafsson, B., & Nissen, P. E. 1989, *A&A*, **219**, L15
- Van Eck, S., Goriely, S., Jorissen, A., & Plez, B. 2003, *A&A*, **404**, 291
- Van Winckel, H., & Reyniers, M. 2000, *A&A*, **354**, 135
- Wiese, W. L., Smith, M. W., & Miles, B. M. 1969, *Atomic Transition Probabilities. Vol. 2: Sodium through Calcium. A Critical Data Compilation* (Washington, DC: National Bureau of Standards)
- Wood, M. P., Lawler, J. E., Sneden, C., & Cowan, J. J. 2014, *ApJS*, **211**, 20
- Woolley, S. E., & Weaver, T. A. 1995, *ApJS*, **101**, 181
- Zacharias, N., Monet, D. G., Levine, S. E., et al. 2004, *AAS Meeting Abstracts*, **205**, 48.15